Effect of artificial length scales in large eddy simulation of a neutral atmospheric boundary layer flow: A simple solution to log-layer mismatch

Tanmoy Chatterjee and Yulia T. Peet

Citation: Physics of Fluids **29**, 075105 (2017); doi: 10.1063/1.4994603
View online: http://dx.doi.org/10.1063/1.4994603
View Table of Contents: http://aip.scitation.org/toc/phf/29/7
Published by the American Institute of Physics

Effect of artificial length scales in large eddy simulation of a neutral atmospheric boundary layer flow: A simple solution to log-layer mismatch

Tanmoy Chatterjee[a] and Yulia T. Peet[b]
Integrative Simulations and Computational Fluids Lab, SEMTE, Arizona State University, Tempe, Arizona 85287, USA

(Received 16 November 2016; accepted 4 July 2017; published online 21 July 2017)

A large eddy simulation (LES) methodology coupled with near-wall modeling has been implemented in the current study for high *Re* neutral atmospheric boundary layer flows using an exponentially accurate spectral element method in an open-source research code Nek5000. The effect of artificial length scales due to subgrid scale (SGS) and near wall modeling (NWM) on the scaling laws and structure of the inner and outer layer eddies is studied using varying SGS and NWM parameters in the spectral element framework. The study provides an understanding of the various length scales and dynamics of the eddies affected by the LES model and also the fundamental physics behind the inner and outer layer eddies which are responsible for the correct behavior of the mean statistics in accordance with the definition of *equilibrium layers* by Townsend. An economical and accurate LES model based on capturing the near wall coherent eddies has been designed, which is successful in eliminating the artificial length scale effects like the log-layer mismatch or the secondary peak generation in the streamwise variance. *Published by AIP Publishing.* [http://dx.doi.org/10.1063/1.4994603]

I. INTRODUCTION

The fidelity of the numerical simulations for very high Reynolds number flows, e.g., atmospheric boundary layer (ABL) with $Re \sim 10^8$–10^{12}, relies on the design of Large Eddy Simulations (LESs)[1,2] with a capability of resolving only scales of a certain order Δ (related to a grid size or a filter size) while modeling the remaining scales smaller than Δ. For high $Re_\tau = u_\tau H/\nu$ [H is the boundary layer (BL) thickness, u_τ is the skin friction velocity, and ν is the kinematic viscosity], rough-wall turbulent shear flows as in the ABL, the grid requirements prohibit the resolution of a viscosity dominated inner layer $\delta_\nu = \nu/u_\tau$ and the scales associated with the aerodynamic roughness $z_0 \ll H$ at the bottom wall. Consequently, shear stress boundary conditions invoking the Monin-Obukov similarity theory[3] instead of no-slip at the bottom wall have been used as a near wall model (cost independent of Re_τ) to emulate the law of the wall (LOTW) in atmospheric boundary layers.

In the near wall modeling LES framework, the dynamics of the smallest Kolomogorov or even the viscous dominated inner layer scales cannot be resolved, limited by the size of the computational grid. The smallest physical velocity and length scales that can be captured correspond to the attached eddies in the inertial layer [$\sim u_\tau$ for velocity scale and $\sim \kappa(z+z_0)$ for length scale that corresponds to a log layer, with $\kappa \approx 0.41$ being the Von-Karman constant and z being the normal distance from the wall[4]]. These length scales are dominant compared to δ_ν and z_0 far away from the viscous wall effects. Apart from the physical length scales, there are additional scales that are generated as an artefact of the subgrid scale (SGS) closure in an LES model and from the numerical grid in certain low order discretizations.[5] Although, both dissipative[6–9] and dispersive[10,11] subgrid scale closure models have been used in the past, a dissipative type of subgrid closures (based on the Smagorinsky model) has gained immense popularity in the last two decades in the simulation of atmospheric flows[12–15] owing to its inherent stabilizing properties in high *Re* simulations while generating reasonably consistent physics in the flow, even without the energy backscatter.[16,17] In particular for a dissipative LES model, a wall-damped standard Smagorinsky model[17] is being used in our current simulations as a less computationally expensive alternative to some other proposed models, such as the turbulent kinetic energy (TKE) two-equation model,[18] equilibrium-based dynamic model,[9] or adaptive Smagorinsky model.[19] For dissipative models, an artificial viscous sublayer due to LES dissipation in the grid will be formed near the wall (see Refs. 1 and 2 for a more comprehensive discussion). The additional effects of filtering in the near-wall modeling would also impose an unphysical scale near the wall. It is thus the interaction of the physical and artificial length scales and the dominance of one over the other that give rise to the near wall dynamics of the flow in numerical simulations.[20]

The predominance of artificial length scales, especially in the near-wall region of high *Re* ABL flows, has been long known to influence the statistics of the near wall region, e.g., the overshoot by 50%–100% of the normalized mean streamwise velocity gradient $\phi(z) = \kappa z/u_\tau \frac{dU}{dz}$ from the theoretical value of one (log law) in the lower 10% of the atmospheric boundary layer, commonly known as the problem of log-layer mismatch (LLM).[9,14,17,20–24] Sullivan *et al.*[14] pointed out that the neutral ABL models have worse results in terms of LLM

[a]Electronic mail: tchatte3@asu.edu
[b]Electronic mail: ypeet@asu.edu.

compared to convective or stably stratified counterparts. LLM is usually attributed to a poor numerical accuracy (numerical dissipation and dispersion associated with insufficient grid resolution in discretization schemes) and inefficient SGS modeling. The elimination of LLM has been partially addressed in the previous literature. The related studies include modifications to the design of the SGS model to incorporate decreasing integral length scales of the near-wall eddies,[9,17,24,25] explicit filtering in the wall closure model,[19,25,26] and deconvolution type reconstruction techniques along with the Smagorinsky type dissipation.[21] More complicated techniques have also been proposed, including optimal control theory,[27] designing high accuracy zones for the law of the wall,[20] and blending functions in self-adaptive Smagorinsky models.[19]

Unlike the previous engineered ways of eliminating the dominance of artificial length scales while addressing LLM, our choice of an efficient LES design for a rough wall-bounded flow (a canonical representation of a neutral ABL) is entirely based on the rudimentary knowledge of associated physical length scales of the turbulent near wall eddies that are affected due to nonlinear dissipative SGS and near wall stress models. A fundamental perception of such length scales acts as a better guidance to control the LES dissipation in a simplified way such that the effect of physical scales can be retrieved in the current study. While the phenomenon of the log-layer mismatch in the mean streamwise velocity gradient and a relatively less known secondary peak generation in streamwise velocity variance seen in experiments are indeed manifestations of the dominance of *artificial length scales* in the flow,[28,29] an incorrect physics behind it cannot be properly analyzed in a coordinate framework in a physical space (x, y, z). Rather, these deficiencies are easier to visualize in a framework where the multiple length scales can be decoupled, since the nonlinearity in the LES model would incur different levels of detriment at different scales of motion. The presence of periodic boundary conditions in the streamwise and spanwise directions in the computation of neutral ABL flows (consistent with the physics due to homogeneity) conveniently allows us to conceive the definition of length scales in a proper way by studying important metrics in turbulence like kinetic energy and shear stress spectra in the wavenumber space.[28,30–32] For example, the inverse of streamwise and spanwise wavenumbers (k_x, k_y), or the wavelengths $\lambda_{x,y} \sim 2\pi/k_{x,y}$, gives an estimate of the length scales of turbulence corresponding to a specified turbulent kinetic energy and a shear stress in the spectra. However, to model the effects of the dynamics of the near wall coherent structures which scale with the wall normal distance z from the wall (e.g., attached eddies[4,33]), the eddy viscosity of the SGS model must be decreased towards the wall to reflect the contribution of smaller integral scales of the near wall eddies that would allow λ_x, λ_y and their scaling laws to be varying with z. The approaches presently proposed in the literature to dynamically control the eddy viscosity near the wall in the neutral ABL simulations, such as scale dependent dynamic Smagorinsky[9,25] or scale adaptive Smagorinsky[19] model, are expensive due to a calculation of eddy viscosity dynamically at every time step and also due to a stringent time stepping requirement for stability compared to their static counterparts. To circumvent this problem, in the current simulation, we resort to a relatively inexpensive method of standard Smagorinsky with Mason and Thompson wall damping[17] for decreasing the eddy viscosity as we move towards the wall. In our current computations, we use an exponentially accurate spectral element discretization in all directions which provides minimum dissipation and dispersion errors asymptotically.[34,35] The previous literature has shown an importance of minimally dissipative numerical schemes for large eddy simulations.[9,36–38] In this regard, the spectral element method (SEM) can be considered as a robust framework for analyzing the performance of the LES models since the length scales involved in the current simulation correspond only to the physical length scales limited by the grid size and the artificial length scales due to the LES approximations.

In the current paper, we investigate the effect of artificial length scales on a neutral ABL (as incurred by the SGS and the near wall LES models), try to understand the nature of the *incorrect physical mechanisms* in the near-wall region that occur due to such scales, and finally, suggest how to choose the LES model parameters in a spectral element framework that can reduce the effect of artificial length scales and replicate the effect of true physical length scales in the flow with reasonable accuracy. Most importantly, our current study also provides a design rubric for standard Smagorinsky SGS closures in a spectral element method based on the least alteration of the true physics observed with these models. Furthermore, the multiscale spectral analysis with different subgrid models provides a basic understanding of the physics of the inner- and outer-layer eddies of the neutral ABL and relates their similarities to the eddies found in high Re channel flows and turbulent boundary layers.[28–32] All the results in our current simulation have been compared against LES results from the previous literature[9,25] or rigorous analytical results of turbulence statistics and spectra corroborated with the moderately high-Reynolds number Direct Numerical Simulation (DNS) data.[30,31,39]

The rest of the paper is organized as follows. First, we document the numerical methods, where we provide the details of the spectral element method and large eddy simulation with the near wall modeling (NWM). Then we provide a short section on the choice of the computational domain with its proper justification, followed by the results and discussion on the statistics and the spectral analysis of the turbulent quantities. At the end, we discuss the conclusions from our key findings.

II. NUMERICAL METHODS

In the computational domain, the 3D incompressible Navier-Stokes equations are solved in a weak formulation using an exponentially accurate higher order spectral element method[40,41] or more specifically Nek5000 (refer to Ref. 42 for details). In this method, the weak formulation of the equations is carried out by a weighted residual technique (orthogonal projection of the residual of the equations), particularly by a Galerkin projection method[42,43] cast using the concept of inner products in functional spaces.

In spectral element methods (SEMs),[40,42,43] the decomposition of the computational domain consists of subdividing $\bar{\Omega} = \Omega \cup \partial\Omega$ into E non-overlapping adjacent rectilinear

elements such that $\bar{\Omega} = \cup_{e=1}^{E}\Omega_e$. Each Ω_e is an image of a reference subdomain under a mapping $\mathbf{x}^e(\mathbf{r}) \in \Omega_e \rightarrow \mathbf{r} \in \hat{\Omega}$, with a well defined inverse $\mathbf{r}^e(\mathbf{x}) \in \hat{\Omega} \rightarrow \mathbf{x} \in \Omega_e$, where the 3D reference subdomain is $\hat{\Omega} = [-1, 1]^3$. Scalar functions within each local element Ω_e are represented as the Nth order tensor product polynomials on a reference subdomain $\hat{\Omega}$. A consistent approach of using spectral element discretization involves using polynomial orders of pressure interpolants (basis functions) two orders lower than the velocity interpolants. This is done in part to remove the spurious modes of pressure along the lines of a finite volume approach.[41,43] With such decomposition, a choice of the functional spaces of velocity and pressure fields is known as $\mathbb{P}_N - \mathbb{P}_{N-2}$ formulation.[43] In 3D, the velocity function in the spectral element method in an element can be expressed as follows:

$$u^e(r_1, r_2, r_3)|_{\hat{\Omega}} = \sum_{i=0}^{N_x}\sum_{j=0}^{N_y}\sum_{k=0}^{N_z} u^e_{ijk}\pi_{N_x,i}(r_1)\pi_{N_y,j}(r_2)\pi_{N_z,k}(r_3), \quad r_1, r_2, r_3 \in [-1, 1]^3, \tag{1}$$

where $\pi_{N_x,i}(r_1)$, $\pi_{N_y,j}(r_2)$, $\pi_{N_z,k}(r_3)$ are the Lagrange polynomial based interpolants of degree N_x, N_y, and N_z. Identically the pressure function in the SEM in the local element with $\pi^p_{N,j}(\zeta) \in \mathbb{P}_{N-2}(\zeta)$ can be given as

$$p^e(r_1, r_2, r_3)|_{\hat{\Omega}} = \sum_{i=1}^{N_x-1}\sum_{j=1}^{N_y-1}\sum_{k=1}^{N_z-1} p^e_{ijk}\pi^p_{N_x,i}(r_1)\pi^p_{N_y,j}(r_2)\pi^p_{N_z,k}(r_3), \quad r_1, r_2, r_3 \in [-1, 1]^3. \tag{2}$$

In the current formulation, we use $N_x = N_y = N_z = N$. The time discretization of the Navier-Stokes solver in the current spectral element code Nek5000[44] involves a 3rd order backward difference/extrapolation scheme (BDF/EXT) with operator integrator factor splitting (OIFS) based characteristic time-stepping. The code is fully dealiased using the 3/2 rule,[45,46] the velocity is solved using the preconditioned conjugate gradient (CG) method, and the pressure solver uses the iterative generalized mean residual solver (GMRES) method in the Krylov subspace.

A. Large eddy simulation: Subgrid scale modeling

The spatially filtered 3D Navier-Stokes equations for large eddy simulation of neutral ABL flows can be obtained by incorporating a convolution integral filter on the original Navier-Stokes equations

$$\frac{\partial\widetilde{\mathbf{u}}}{\partial t} + \widetilde{\mathbf{u}}\,\nabla\,\widetilde{\mathbf{u}} + \frac{1}{\rho}\nabla\widetilde{p^*} - \widetilde{\mathbf{F}} - \nu\nabla^2\widetilde{\mathbf{u}} = -\nabla\cdot\boldsymbol{\tau}^{SGS}(\widetilde{\mathbf{u}}, \widetilde{\mathbf{u}}). \tag{3}$$

The subgrid stress (SGS) tensor in Eq. (3), $\boldsymbol{\tau}^{SGS}(\widetilde{\mathbf{u}}, \widetilde{\mathbf{u}}) = \widetilde{\mathbf{u}\mathbf{u}^T} - \widetilde{\mathbf{u}}\widetilde{\mathbf{u}}^T$ arising from the non-commutativity of filtering with the nonlinear advection term, is modeled using a Smagorinsky type eddy viscosity closure

$$\boldsymbol{\tau}^{SGS} - \frac{1}{3}tr(\boldsymbol{\tau}^{SGS})\mathbb{I} = -2\nu_t\nabla^s\widetilde{\mathbf{u}}, \tag{4}$$

where $\nabla^s\widetilde{\mathbf{u}} = \frac{1}{2}(\nabla\,\widetilde{\mathbf{u}} + \nabla\,\widetilde{\mathbf{u}}^T)$ is the filtered stain rate and $\mathbb{I}$ is the identity tensor. In the classical Smagorinsky model, the eddy viscosity is given by

$$\nu_t = (l_f)^2|\nabla^s\widetilde{\mathbf{u}}|, \tag{5}$$

where $|\nabla^s\widetilde{\mathbf{u}}| = (2\nabla^s\widetilde{\mathbf{u}} : \nabla^s\widetilde{\mathbf{u}})^{1/2}$. The filter length scale l_f is assumed to be proportional to the grid filter width (cutoff scale) Δ, $l_f = C_s\Delta$, and C_s is the non-dimensional Smagorinsky coefficient. According to Ref. 16, l_f can also be interpreted as the mixing length of the subgrid scale eddies (l_f is usually less than Δ justifying the name "subgrid scale"). The grid filter width here is calculated as $\Delta = (\Delta x\Delta y\Delta z)^{1/3}$,[47] where $\Delta x, \Delta y, \Delta z$ are taken at the Gauss-Lobatto-Legendre (GLL) nodes as the weighted averages of the node distances (analogous to a central difference scheme) at the element interior and one sided difference at the element boundaries. For high Reynolds number turbulent ABL flows, we use near wall algebraic wall damping functions by Mason and Thomson,[17]

$$\frac{1}{l_f^n} = \frac{1}{(C_0\Delta)^n} + \left\{\frac{1}{\kappa(z + z_0)}\right\}^n, \tag{6}$$

or written directly in terms of the Smagorinsky coefficient,

$$\frac{1}{C_s^n} = \frac{1}{C_0^n} + \left\{\frac{\Delta}{\kappa(z + z_0)}\right\}^n. \tag{7}$$

Equation (6) essentially represents an *ad hoc* blending function with parameters C_0, n such that the filter length scale saturates at $l_f(z) \sim C_0\Delta$ at the outer layer while retrieving Prandtl's mixing length $l_f(z) \sim \kappa(z + z_0)$ as we approach the wall. While C_0 controls the asymptotic value of $l_f(z)$, n controls the shape or the growth rate of $l_f(z)$ in the inner layer as we will see later. Here κ is the Von-Karman constant and $z_0 \ll H$ is the aerodynamic roughness length of the bottom "wall," where H is the boundary layer thickness.

B. Model assumptions: Boundary conditions

We incorporate periodic boundary conditions in the streamwise and spanwise directions while the top boundary conditions are stress free: $\partial\widetilde{u}/\partial z = \partial\widetilde{v}/\partial z = 0$ and $\widetilde{w} = 0$, where $\widetilde{u}, \widetilde{v}, \widetilde{w}$ are the resolved streamwise, spanwise, and wall normal velocities. At the bottom surface, we use a wall stress boundary condition without having to resolve the rough wall,[48] relating the wall stress vector to the in-plane horizontal velocity vector $\widetilde{\boldsymbol{u}}_h$ at the first half-node from the wall using the standard Monin-Obukhov similarity law[3] along with no-penetration conditions of large eddies, $\widetilde{w} = 0$,

$$\frac{1}{\rho}\boldsymbol{\tau}_s = -\kappa^2\frac{\widehat{\widetilde{\boldsymbol{u}}}_{h,\frac{\Delta z}{2}}(x, y, t)\,|\,\widehat{\widetilde{\boldsymbol{u}}}_{h,\frac{\Delta z}{2}}|(x, y, t)}{\log(\frac{z}{z_0})\Big|^2_{\frac{\Delta z}{2}}}, \tag{8}$$

where $|\,\widehat{\widetilde{\boldsymbol{u}}}_{h,\frac{\Delta z}{2}}| = \sqrt{\widehat{\widetilde{u}}^2_{\frac{\Delta z}{2}} + \widehat{\widetilde{v}}^2_{\frac{\Delta z}{2}}}$ and $\widehat{\widetilde{\boldsymbol{u}}}_{h,\frac{\Delta z}{2}} = \widehat{\widetilde{u}}_{\frac{\Delta z}{2}}\vec{e_x} + \widehat{\widetilde{v}}_{\frac{\Delta z}{2}}\vec{e_y}$ ($\vec{e_x}, \vec{e_y}$ are unit vectors in the x, y directions). The "hat" represents additional explicit filtering carried out in the modal space by attenuating $k_c = 4$, highest Legendre polynomial modes of the spectral element model (please refer to Appendix A for the description of the explicit filtering method). This explicit filtering is done along the lines of Refs. 19 and 25 to control the log-layer mismatch and to bound the wall shear stress. For collocated spectral element methods, $\widehat{\widetilde{u}}_{\frac{\Delta z}{2}}$, $\widehat{\widetilde{v}}_{\frac{\Delta z}{2}}$ are calculated as an interpolation at half wall node $\Delta z/2$, i.e., between $\widehat{\widetilde{u}}(x, y, 0, t)$ and $\widehat{\widetilde{u}}(x, y, z = \Delta z, t)$ (and similar procedure for $\widehat{\widetilde{v}}$). The aerodynamic roughness is $z_0 = 10^{-4}H$ which corresponds

to the previous literature.[9,19] Existing literature on near wall modeling[9,12,19,47,49–51] has generally used vertically staggered finite-difference schemes when using stress boundary conditions for rough wall models with $\Delta z/2$ being a physical grid distance of the horizontal velocities away from the wall. The present paper incorporates a new methodology for rough wall modeling using the collocated spectral element method, which is reflected in Eq. (8). Our spectral element model for shear stress developed using weak formulation is physically consistent, where the wall model essentially acts as a momentum flux closure scheme (see Appendix B for a mathematical formalism of stress boundary conditions in the SEM method).

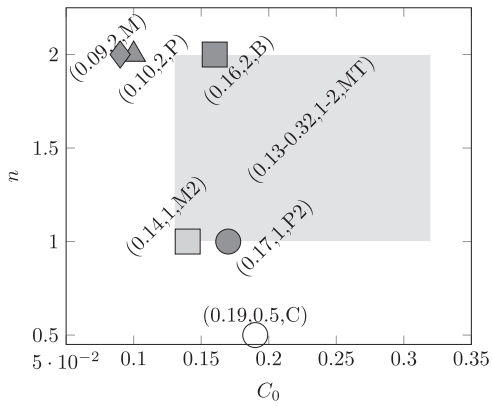

FIG. 2. Values of $\{C_0, n\}$ tuple used in the past literature in a parametric space for the wall-damped Smagorinsky model. *MT* (gray rectangular patch)—Mason and Thomson;[17] *P*, *P*2—Porté-Agel *et al.*;[9] *B*—Bou-Zeid *et al.*;[25] *M*—Meyers;[26] *M*2—Wu and Meyers.[19] *C* is the $\{C_0, n\}$ parameter tuple recommended in our paper for the standard wall-damped Smagorinsky model with SEM. $\{C_0, n\}$ corresponding to *B*, *C*, *M*, and *P*2 are used in current simulations.

III. PROBLEM FORMULATION

A. Choice of LES parameters

In order to analyze the subgrid-scale model given by Eqs. (4)–(7), we plot the dependence of the Smagorinsky coefficient C_s from Eq. (7) on the vertical distance z in Fig. 1. The purpose of our analysis is to choose the appropriate values of the subgrid-scale model parameters C_0 and n to use in spectral-element methods in high-Reynolds number simulations of a neutral atmospheric boundary layer. Large eddy simulations in a continuous Galerkin based SEM with Smagorinsky-type models are not extensive in the community,[52,53] and even though some recent studies by Lodato and co-workers[54,55] have explored moderate Reynolds number LES in a discontinuous flux based SEM framework, the authors do not know any attempts to use these methods in the context of very high Reynolds numbers and atmospheric boundary layer flows. As discussed earlier, the value of C_0 controls the asymptotic value of the Smagorinsky coefficient C_s away from the wall. In order to understand the influence of the parameter n, the values of C_s for a fixed value of $C_0 = 0.16$ and different values of $n = 0.5$, 1, 2 are plotted in Fig. 1(a). Note that this plot is grid-dependent (as Δ is grid-dependent), and Fig. 1 is plotted for the baseline SEM grid ($30 \times 20 \times 24$ elements) used in the current simulations. We see that although the slope of C_s in the limit of $z \to z_{wall}$ does not depend on n which can also be understood from a previously discussed near-wall scaling of $l_f(z) \sim \kappa(z + z_0)$, the value of n controls the growth of C_s in the inner layer and, specifically, lower values of n result in a slower growth of C_s and a longer vertical distance it takes for C_s to saturate to its asymptotic value of C_0. This slow growth introduces a physically relevant dependence of C_s on z/Δ in the inner layer that results in correct near-wall dynamics and represents consistent trends of filter scales with grid-refinement. It is thus understandable that, in order to provide comparable dissipation length scales in the outer region, higher values of C_0 are usually used with lower values of n: $C_0|_{n=0.5} > C_0|_{n=1} > C_0|_{n=2}$. This is indeed reflected in the choice of parameters C_0 and n reported in the previous literature[9,17,25,26,56] and summarized here in a parametric form in Fig. 2. The dependence of C_s versus z for the current choice of parameters is shown in Fig. 1(b). In addition to standard values of $n = 1$, 2, we also propose to explore a lower value of $n = 0.5$ ($\{C_0, n\} = \{0.19, 0.5\}$) than that reported in the previous literature, which corresponds to a slower growth of C_s in the inner layer and provides a better control of near-wall dissipation length scales. We will show in the current paper that this model indeed performs remarkably well in the SEM LES of atmospheric boundary layer flows. It is interesting to note that the slower inner growth of C_s corresponding to $C_0 = 0.19$, $n = 0.5$ is similar to the dynamic models of Porté-Agel.[9] In addition, we also consider an extremely low value of $C_0 = 0.09$ with $n = 2$ similar to Ref. 26 in our simulations and show that attempts to control the near-wall dissipation by lowering the value of C_0 without changing the near-wall growth of C_s (determined by n) results in an unphysical turbulence in the current spectral-element method.

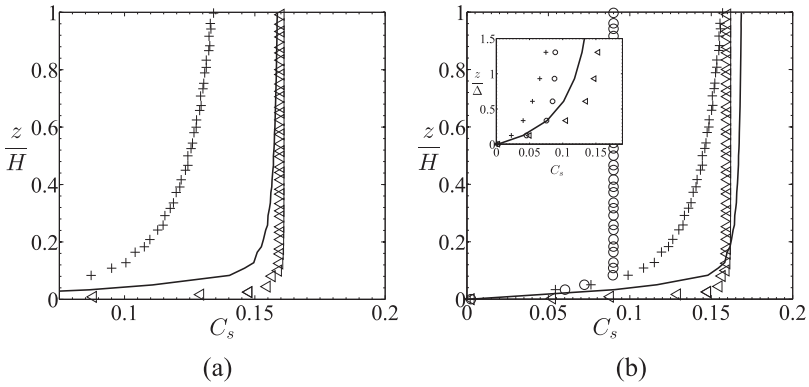

FIG. 1. Smagorinsky coefficient C_s vs z/H for the current SEM grid ($30 \times 20 \times 24$ elements). (a) $C_0 = 0.16$ (fixed) $n = 0.5$, 1, 2. ◁, $n = 2$; –, $n = 1$; +, $n = 0.5$. (b) ◁, $C_0 = 0.16$, $n = 2$; –, $C_0 = 0.17$, $n = 1$; +, $C_0 = 0.19$, $n = 0.5$; ○, $C_0 = 0.09$, $n = 2$; Inset: variation of C_s vs z/Δ, zoomed-in. $\kappa = 0.41$, von Karman constant; $z_0 = 10^{-4}H$, aerodynamic roughness length.

TABLE I. Suite of LES cases for the neutral ABL flow involving parametric variation. k_c is the number of modes of cutoff filter per element in explicit filtering of the NWM (see Appendix A) and N is the order of Lagrange-Legendre polynomial in each element. $\{C_0, n\}$ are the tuning parameters of the wall-damped Smagorinsky SGS model.

Case	k_c/N	$\{C_0, n\}$
$C_0^{16} n^2 k_c^{2/7}$ (I)	2/7	{0.16, 2}
$C_0^{16} n^2 k_c^{4/7}$ (IIa)	4/7	{0.16, 2}
$C_0^{9} n^2 k_c^{4/7}$ (IIb)	4/7	{0.09, 2}
$C_0^{16} n^2 k_c^{6/7}$ (III)	6/7	{0.16, 2}
$C_0^{17} n^1 k_c^{2/7}$ (IV)	2/7	{0.17, 1}
$C_0^{17} n^1 k_c^{4/7}$ (V)	4/7	{0.17, 1}
$C_0^{17} n^1 k_c^{6/7}$ (VI)	6/7	{0.17, 1}
$C_0^{19} n^{05} k_c^{2/7}$ (VII)	2/7	{0.19, 0.5}
$C_0^{19} n^{05} k_c^{4/7}$ (VIII)	4/7	{0.19, 0.5}
$C_0^{19} n^{05} k_c^{6/7}$ (IX)	6/7	{0.19, 0.5}

Considering also the variation in the filtering parameter k_c in the near-wall model as discussed in Sec. II B, Table I summarizes the list of cases investigated in the current paper involving a parametrically varying wall-damped Smagorinsky model. It must be noted that both the Smagorinsky length scale l_f and the cutoff modes k_c in the near-wall model incorporate artificial length scales into our flow simulations. Our purpose is to analyze the behavior of the numerical models in the presence of these artificial length scales from the perspective of physics and develop a *robust* and *physically consistent* ABL model in the context of spectral elements.

B. Computational domain

The computational domain is taken to be $2\pi H \times \pi H \times H$ as in Ref. 19, with $Re = U_\infty H/\nu = 10^{10}$, where U_∞ is the streamwise velocity outside of the boundary layer. The size of the computational domain ensures a sufficient decay of the streamwise auto-correlation length scale necessary to make periodic boundary conditions consistent[57–59] and is also able to capture the appropriate scaling laws of the attached eddies[4,33] as reported in the previous DNS literature.[30,31] The discretization parameters of the computational domain are presented in Table II. N_i^e represents the number of elements in the ith direction and N_{xyz} is the global number of grid points used in the computation. Also, Δ_x/Δ_z, Δ_x/Δ_y are the aspect ratios of the spectral elements, where Δ_x, Δ_y, Δ_z are the sizes of the spectral elements in the respective directions. We use 7th order Lagrange-Legendre polynomials as the basis functions resulting in 8^3 collocation nodes per element. All the analyses involving the statistics and spectra in Secs. IV A–IV D are carried out for the baseline grid in Table II. However the LES simulations have also been tested for five other coarsened or refined grids for the *grid sensitivity* analysis in order to support the robustness of the wall modeled LES. The detailed results of the grid sensitivity can be found in Appendix C.

TABLE II. The baseline grid parameters for LES of atmospheric boundary layers.

$N_x^e \times N_y^e \times N_z^e$	N_{xyz}	Δ_x/Δ_z	Δ_x/Δ_y	$\Delta z/z_0$
$30 \times 20 \times 24$	5.02×10^6	5.0265	1.33	27

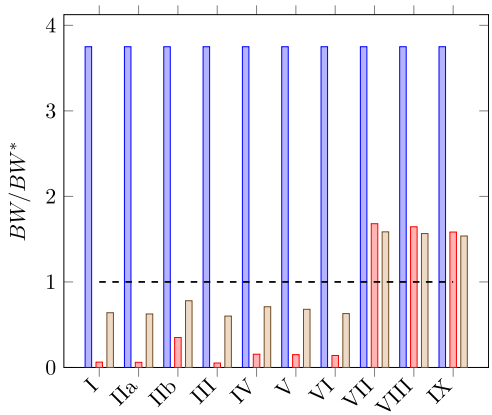

FIG. 3. Three BW parameters[20] compared to their critical value $BW^* = \left\{N_\delta^*, \Re^*, R_{LES}^*\right\}$ plotted in a bar chart as BW/BW^* in our current wall-damped Smagorinsky model for the baseline grid ($30 \times 20 \times 24$ elements). Blue (left): N_δ/N_δ^*; red (middle): $\Re/\Re^*$; brown (right): R_{LES}/R_{LES}^*. Black – – is the threshold $BW/BW^* = 1$ above which the results are considered in a high-accuracy zone.[20] Please refer to Table I for case numbering.

The minimum grid point wall-normal distance is $\Delta z/z_0 \gtrapprox 20$, manifesting that the first grid node does not resolve the geometric roughness and lies in the log-law of the wall, consistent with wall modeling conceptualizations.[19] All the grids designed for the current *ABL* are refined beyond the critical grid resolution required for an accurate representation of the mean streamwise velocity statistics, as discussed by Brasseur and Wei.[20] The three parameters, identified by Ref. 20 (hereby referred to as BW parameters) used for designing a high-accuracy zone (HAZ), are (a) N_δ, the vertical grid resolution in the domain; (b) $\Re$, the ratio of the turbulent shear-stress to the total stress in the first grid point from the wall; and (c) R_{LES}, i.e., the Reynolds number based on the SGS eddy viscosity. According to Brasseur and Wei,[20] these three parameters need to be greater than some critical value to be in the HAZ. For brevity, we show the BW parameters for the different Smagorinsky based SGS models in Fig. 3 only for the baseline grid. However, the conclusions can be generalized for all the grids from Table VI in Appendix C. The vertical resolution in spectral elements ensures that N_δ is well above the critical value $N_\delta^* \sim 45$–50. The other two parameters, $\Re$ and R_{LES}, are SGS model dependent and are only above their critical values indicating the appropriate accuracy of the model, for cases VII-IX ($C_0^{19} n^{05} k_c^{2/7}$, $C_0^{19} n^{05} k_c^{4/7}$, $C_0^{19} n^{05} k_c^{6/7}$). For collecting statistics presented in the manuscript, the statistical stationarity of the neutral ABL simulations was first ensured after $\sim 45 T_e$, where $T_e = 2\pi H/U_\infty$ is the flow through time, upon which the temporal averaging of statistics and collection of instantaneous snapshots for spectral analysis have been carried out for 120 T_e time units.

IV. RESULTS AND DISCUSSION

In this section, we provide a detailed comparison of the results involving the mean and turbulent statistics of our LES computations with the data from the previous literature.[9,25] The results are further corroborated by a rigorous multi-dimensional spectral analysis that elucidates the flow

physics in the inner and outer layers. Investigation of the results involving the statistics and the spectra of our LES computations helps us suggest an accurate and reliable LES-NWM model for spectral element computations, which can emulate the correct physics of the eddies in wall-bounded turbulence. The results have been further supported by the grid sensitivity analysis (see Appendix C for details) which indicates that our conclusions are grid invariant and the statistics has a leading order effect from the wall model LES and not from the grid itself.

A. Law of the wall: Generation of log-layer mismatch

The theory of turbulent flows suggests that a well-defined region of a logarithmic dependence of the mean streamwise velocity on the vertical distance from the wall (log-law) persists due to dominance of inertial scales in the inner layer corresponding to the lower 10% of the boundary layer, $z/H \sim 0.1$.[58] The log-law can be compactly represented in terms of the non-dimensional streamwise velocity gradient, $\phi(z) = \kappa z/u_\tau dU/dz$, which attains a value of one in the log layer [$\phi(z) = \kappa z/u_\tau dU/dz$, $z/H \leq 0.1$] and deviates from one with $\phi(z) > 1$, $d\phi(z)/dz \neq 0$ beyond the inner layer depicting the so-called wake region (for more details of the logarithmic regime in high *Re* wall bounded turbulence, see, for example, a review by Smits *et al.*[29]). Figures 4(a)–4(d) show that except for cases $C_0^{19}n^{05}k_c^{j/7}$ $j = 2, 4, 6$, all the current LES models develop strong deviations from the logarithmic trend of as much as 40%-60% at $z/H < 0.1$ known as the *log-layer mismatch* (LLM). As was shown in the work of Brasseur and Wei,[20] these log-layer mismatches in LES are likely to occur due to the presence of an *artificial LES viscous sublayer*. Similar to physical log-law deviations due to the viscous sublayer in smooth-wall channel flows,[57,60] a numerical viscosity (i.e., due to a subgrid turbulent viscosity and other algorithmic additions to the dissipation) creates a numerical frictional layer that causes the overshoot. Interestingly, as the true viscous overshoot scales with the viscous units (ν/u_τ) showing the same location of the peak overshoot versus z^+ for different Reynolds numbers,[57,60] the LES overshoot scales with the "LES viscosity" (ν_{LES}/u_τ) showing the collapse of the velocity gradient curves in the inner layer if plotted with these z^+_{LES} units.[20]

The manifestation of similar effects in our simulations with the wall-damped Smagorinsky model is evident in Fig. 4. We can see that decreasing C_0 to 0.09 from 0.16 with $n = 2$ fixed (case $C_0^{16}n^2k_c^{4/7}$ vs $C_0^{09}n^2k_c^{4/7}$) decreases the overall eddy viscosity in the LES computation, shifting the LLM peak from $z/H = 0.05$ to $z/H = 0.02$ towards the wall as seen in Fig. 4(c) indicating the shorter extent of the LES eddy viscosity sublayer. The peaks of the log-layer mismatch in Fig. 4 from our current SEM simulations are closer to the wall compared to the standard Smagorinsky model in the literature.[9,19,25] We point out that in cases $C_0^{19}n^{05}k_c^{j/7}$ $j = 2, 4, 6$, the dissipation is low enough that the inertial scales $\sim\kappa z$ dominate over artificial viscous scales, which completely eliminates the formation of the artificial sublayer and hence the LLM.

1. Effect of k_c in the near wall model

The effect of explicit filtering in the near wall model is not very conspicuously observed in the near-wall region, $z/H < 0.1$, even though differences are visible in the far outer layer. Explicit filtering retains the large-scale near-wall velocity structures for the model while filtering out the smaller scales near the SGS limit. The fact that the log-law of the wall has its significant contribution from the larger scales of

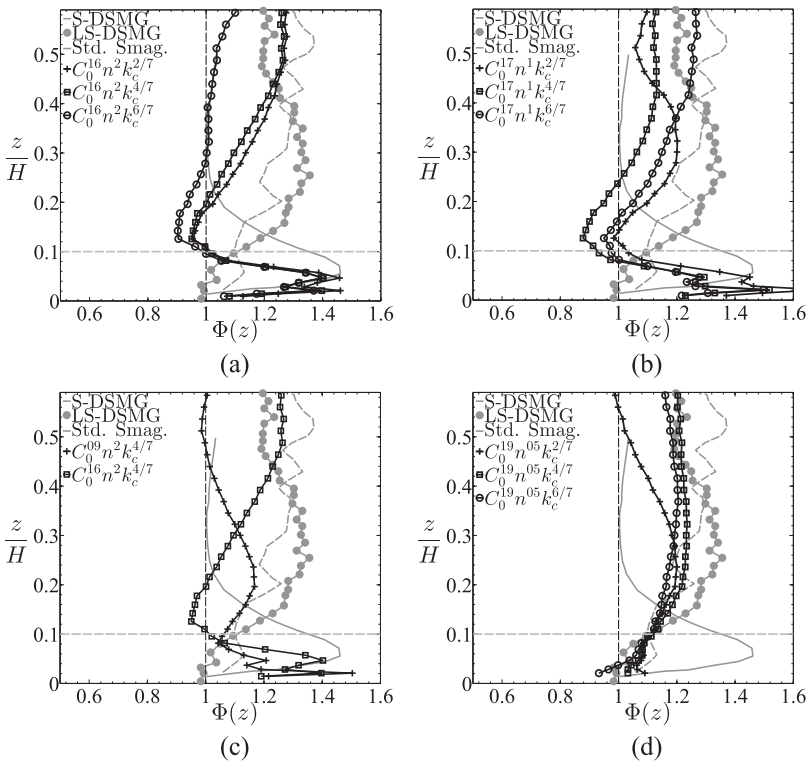

FIG. 4. Temporally and horizontally averaged normalized mean streamwise velocity gradient $\Phi(z)$ vs z/H for SGS parameters. (a) Cases $C_0^{16}n^2k_c^{j/7}$, $j = 2, 4, 6$, (b) cases $C_0^{17}n^1k_c^{j/7}$, $j = 2, 4, 6$, (c) cases $C_0^{\xi}n^2k_c^{4/7}$, $\xi = 16, 9$, and (d) cases $C_0^{19}n^{05}k_c^{j/7}$, $j = 2, 4, 6$. LS-DSMG: Lagrangian scale dependent dynamic Smagorinsky model, Bou-Zeid *et al.*;[25] Std. Smag. (Standard Smagorinsky), Bou-Zeid *et al.*;[25] S-DSMG: spatially averaged scale dependent dynamic Smagorinsky model, Porté-Agel *et al.*[9] The dashed-gray line is demarcation between the inner and outer layers.

motion[29,39] is manifested in the slight reduction of the log-layer mismatch, with increasing the cutoff modes in filtering k_c/N, from 2/7 to 4/7 [see Figs. 6(b) and 6(c)]. However excessive filtering on horizontal velocity, especially in models where artificial viscous layer is not formed (cases $C_0^{19}n^2k_c^{j/7}$ $j = 2, 4, 6$), can contribute to the underdissipative negative log-layer mismatch as in Fig. 6(b) for $k_c = 6/7$. However, further studies of this effect are needed to form a more complete description.

B. Reynolds stresses

For completeness of the discussion, we present the results of the second order moments before moving on to the discussion of the spectral analysis in Sec. IV C. A comparison of the streamwise variance for the different model parameters of the wall-damped Smagorinsky model with previously published numerical simulations[9] and laboratory scale experiments[28] can be found in Fig. 5. To better understand the near-wall analytical scalings of the variances, Fig. 6 shows some of the resolved second order moments or Reynolds stresses for various parametric cases of the Smagorinsky based LES model in a logarithmic plot. Perry *et al.*[33,61] performed a detailed analysis of the overlap regions in the spectra of $\widetilde{u'^2}, \widetilde{v'^2}, \widetilde{w'^2}, -\widetilde{u'w'}$ for wall-bounded turbulence through the theory of an *equilibrium layer* supported by their hot-wire experiments. They found the evidence of a logarithmic trend in the streamwise and spanwise variance profiles, as well as a flat trend (independence on z) in the wall normal variance and in the kinematic shear stress in the near wall region $z/H < 0.1$. Such logarithmic trends of streamwise variance (observed only in $C_0^{09}n^2k_c^{4/7}$, $C_0^{19}n^{05}k_c^{4/7}$) were also documented in later experiments of wall bounded turbulence using hot wires[28] and in the LES computations of rough wall ABL.[24] In our computations, it is only for the case $C_0^{19}n^{05}k_c^{4/7}$ that we observe *correct* logarithmic trends of streamwise *and* spanwise variances, as well as flat trends of wall normal variance and kinematic shear stress in the near wall region $z/H \sim 10^{-2}$–10^{-1} [see Fig. 6(d)]. Interestingly, a similar effect of an artificial secondary peak generation in streamwise variance is also observed in some experiments[28,29] due to the presence of *artificial length scale* effects in hot wire probes.

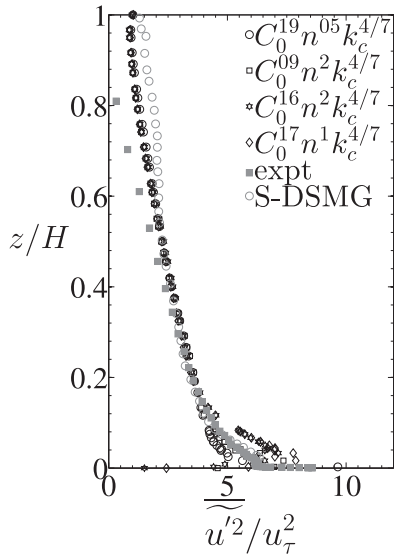

FIG. 5. Horizontally averaged resolved streamwise variance $\widetilde{u'^2}$ normalized with u_τ^2 for different Smagorinsky based SGS models $C_0^{16}n^2k_c^{4/7}$, $C_0^{17}n^1k_c^{4/7}$, $C_0^{09}n^2k_c^{4/7}$, and $C_0^{19}n^{05}k_c^{4/7}$ compared against scale-dependant dynamic Smagorinsky (S-DSMG)[9] model and wind tunnel experiment.[28]

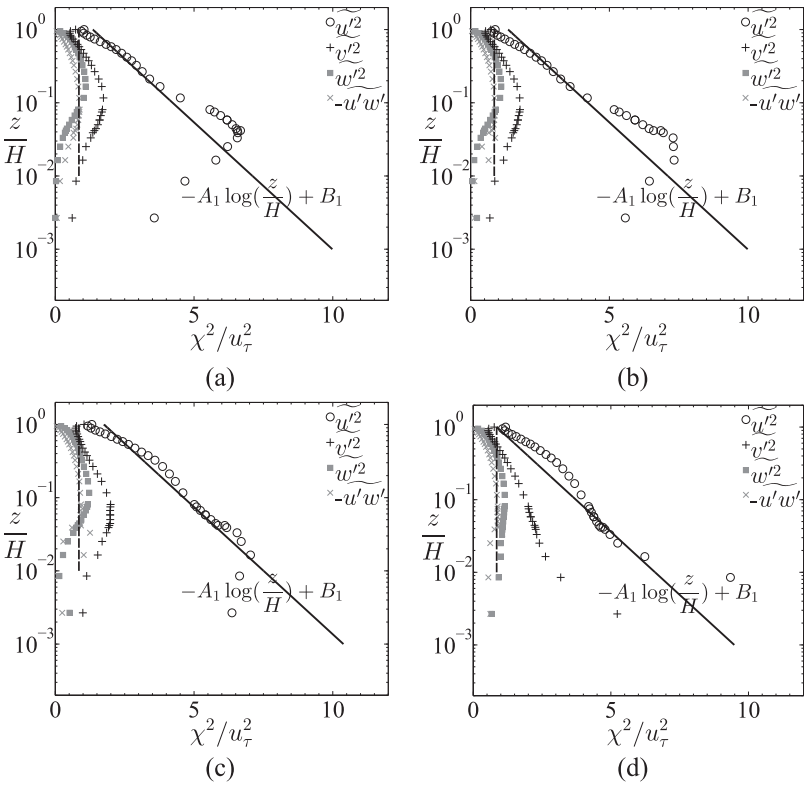

FIG. 6. Variation of horizontally averaged resolved second order moments $\chi^2 = \widetilde{u'^2}, \widetilde{v'^2}, \widetilde{w'^2}, -\widetilde{u'w'}$ with z/H for different models. (a) Case $C_0^{16}n^2k_c^{4/7}$, (b) case $C_0^{17}n^1k_c^{4/7}$, (c) case $C_0^{09}n^2k_c^{4/7}$, and (d) case $C_0^{19}n^{05}k_c^{4/7}$. Solid black line: log-trend of streamwise variance, $A_1 = 1.25$ is the slope of the logarithmic trend.[24,33] Dashed black line: flat trend of kinematic shear-stress—equilibrium layer.

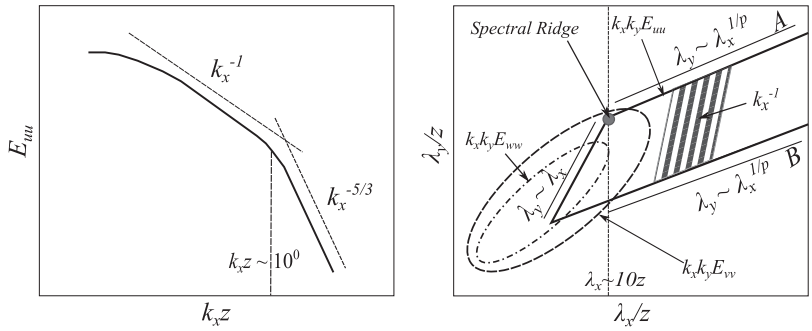

FIG. 7. (a) A schematic of a near-wall 1D u spectra, depicting the scaling laws and indicating the regions of k_x^{-1} and $k_x^{-5/3}$ scaling. (b) A schematic of near-wall 2D premultiplied u, v, w energy spectra, with the linear scaling $\lambda_y \sim \lambda_x$ and the power law $\lambda_y \sim \lambda_x^{1/p}$ scaling shown for u spectra. Both 1D and 2D spectra are representatives of the near-wall phenomenon. A spectral ridge corresponds to a change of scaling from linear to power-law.

C. Effect of length scales: Spectral analysis

The spectral analysis of wall-bounded turbulence illustrates a clear picture of the dynamics of turbulent eddies (see the review by Jiménez[39]) responsible for the specific mean and turbulent statistics as discussed in Secs. IV A and IV B.

In a statistical sense, the near-wall dynamics of high Re turbulence is made up of a hierarchy of self-similar coherent active wall normal motions, bearing Reynolds stresses[4,32,33,61–63] whose length scales $\lambda_x \sim O(z)$ and the velocity scales $\sim O(u_\tau)$. Apart from these eddies, also present are the quasi-inviscid, anisotropic, and horizontal inactive eddies with $\lambda_x \gg O(z)$, "attached" in the sense of Townsend.[4] These inactive motions at distance z from the wall can also be thought of as being "active" at wall distances $z_\lambda \gg z$, where z_λ is the vertical wall distance of the order of the length scale of *inactive motions*.[39] Larger coherent flow organizations in wall-bounded turbulence, e.g., large scale motions (LSMs $\sim 3H$) and very large-scale motions (VLSMs $\gg 3H$), carrying almost 50% of the kinetic energy and Reynold's stresses are beyond the scope of this paper, mainly due to a shorter computational domain, and hence are not discussed here (for more details on LSM's and VLSM's, please see Refs. 29, 32, and 63–65).

Strong analytical and experimental evidence of two distinct "overlap" regions in the spectra of streamwise and spanwise turbulent intensities $\overline{u'^2}$, $\overline{v'^2}$ and single "overlap" of Kolmogorov scaling for wall-normal turbulence intensity $\overline{w'^2}$ have been found at very high Reynolds number wall-bounded flows.[33,61,66] The overlap between the integral and the *attached eddy* length scales gives rise to the k_x^{-1} scaling in streamwise energy spectra, while the overlap between the *attached eddy* and viscous/Kolmogorov scales gives rise to the Kolmogorov $k_x^{-5/3}$ law of the cascade,[33,58] with k_x being the streamwise wave number [see the schematic in Fig. 7(a)]. Despite some debate on the existence of the k_x^{-1} spectra,[31,67,68] hot wire experiments in Refs. 28 and 69–71 have shown that for moderately high Re wall-bounded turbulence, a decade of range in the inverse law spectra can be observed in the near wall regime, at around $z/H \lesssim 0.01$–0.02. Additionally, the data from the previous literature also indicate a consistent region of $k_x^{-1/2}$ scaling at larger scales, or smaller wavenumbers $k_x z$, before the "well-documented" k_x^{-1} region, at high Re atmospheric surface layer experiments[72–75] and neutral atmospheric boundary layer simulations.[9,26] Although this region was not explicitly discussed in the previous literature, we find strong evidence of this scaling predicted by our best-performing SGS model, $\{C_0, n\} = \{0.19, 0.5\}$, and present some additional results in support of this.

A more supportive picture can be obtained in the two-dimensional spectra scenario, for example, looking at a 2D energy spectrum premultiplied by wavenumbers k_x, k_y, as in the schematic of Fig. 7(b). A self-similar linear-scaling $\lambda_y \sim \lambda_x$ exists for length scales $\lambda_x \lesssim 10z$, which corresponds to the *active wall-normal motions*. These motions are three dimensional motions due to the presence of vertical energy (E_{ww}) spectra. The regime of larger length scales, $\lambda_x \gtrsim 10z$ ($k_x z \sim 10^0$), where the power-law scaling is present, corresponds to the *attached inactive motions*, which are mainly horizontal motions, as seen from the long-wavelength cutoff of vertical energy, E_{ww}, spectra. (For more details of "**active and inactive motions**," see Refs. 4, 74, 76, and 77.) The basis of this power-law behavior $\lambda_y \sim (\lambda_x)^{1/p}$ has been discussed in detail in Refs. 30 and 31 and is mainly attributed to the effects of long-time dispersion of flow structures in background turbulence. While $p = 3$ scaling occurs at low-speed regions of the near wall streaks, dominated by shear, the $p = 2$ scaling is more generic and is not only formed at high-speed regions of the near wall streaks, dominated by a uniform momentum, but also due to the dissipation in the outer layer. Figure 8(a) shows the near-wall streaky flow, which has completely different flow structures than the outer layer in Fig. 8(b), the latter being populated by much larger eddies and is less coherent (the snapshots are shown for case $C_0^{19} n^2 k_c^{4/7}$). It is to be noted that for brevity and easy reference, we refer to the power scaling

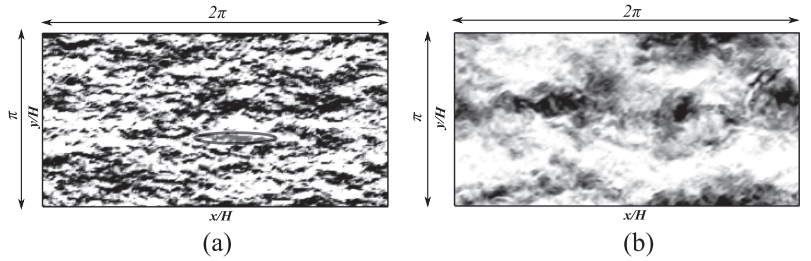

FIG. 8. Time-snapshot of velocity magnitude $\sqrt{u^2 + v^2 + w^2}$, normalized by U_∞ at the xy plane for case $C_0^{19} n^{05} k_c^{4/7}$. (a) Inner layer, $z/H = 0.025$. Black patch: $0.7U_\infty$; white patch: $0.5U_\infty$. (b) Outer layer, $z/H = 0.875$. Black patch: U_∞; white patch: $1.2U_\infty$. Encircled region in (a): low velocity streaky flow, $\lambda_x \sim 16z$.

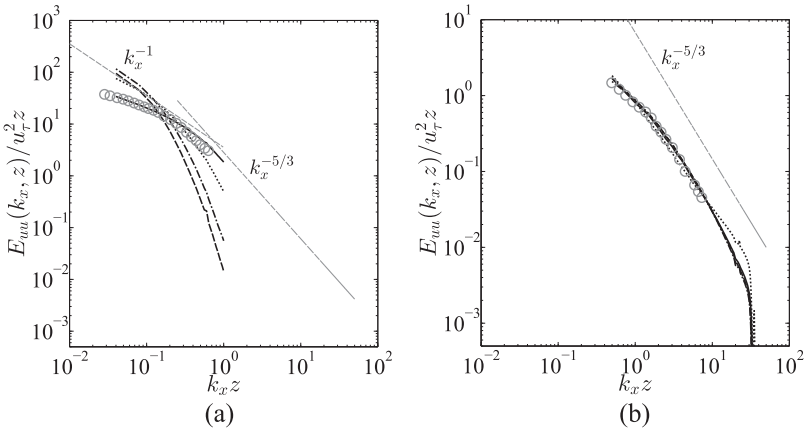

FIG. 9. Normalized streamwise energy spectra $E_{uu}(k_x,z)/u_\tau^2 z$ vs $k_x z$ at different normalized heights. (a) $\xi = z/H = 0.028$ and (b) $\xi = z/H = 0.519$ compared against previous literature.[9] Case $C_0^{16} n^2 k_c^{4/7}$ (dashed line), $C_0^{17} n^1 k_c^{4/7}$ (chain-dotted line), $C_0^{09} n^2 k_c^{4/7}$ (dotted line), $C_0^{19} n^{05} k_c^{4/7}$ (solid line), scale dependant dynamic model[9] (gray circle).

in Fig. 7(b) at the top of the contour as the "***A***" scaling, while that in the bottom of the contour as the "***B***" scaling. It must be appreciated that a part of the region of 2D spectra between the "***A***" and "***B***" power law scaling behavior, corresponding to the *attached inactive motions*, when integrated over the λ_z wavelength, would supposedly generate the classic k_x^{-1} scaling law. More specifically, we would like to mention that the community in favor of the k_x^{-1} scaling[28,33,70,71,75] actually found evidence of this inverse law in the regime of integration just discussed. Additionally, even though the focus of our computational study involves rough walls, previous literature[75,78,79] has consistently shown that smooth wall scaling laws of attached eddies also hold for rough walls and particularly if the roughness length is less than 2.5% of the boundary layer thickness ($z_0/H = 10^{-4}$ in the current simulations) as also predicted by Refs. 80 and 81.

1. 1D spectra

The comparison of the spectra for the LES models in our study (see Table I) will be based on the robust theoretical scaling laws of the active and inactive motions as discussed above since these eddies comprise the most important dynamics of the wall bounded flow. It must be noted that the length scale $\lambda_x \sim 10z$ is the *barrier* between the active and inactive motions. The discussion in this section would not only lead us to the most consistent model corresponding to the correct spectral behavior but also point to the implications of the incorrect scaling laws produced by the other models in terms of numerically *inconsistent physics of the active and inactive eddies*. In the subsequent analysis, the energy spectra and cospectra are calculated as $E_{uu} = \langle \hat{u}\hat{u}^* \rangle$ and $\phi_{uw} = \langle \hat{u}\hat{w}^* \rangle$, where $\hat{}$ denotes the Fourier transform, $*$ denotes the conjugate transpose, and $\langle\rangle$ denotes the temporal averaging.

In Fig. 9, we plot the mean (temporally, horizontally averaged) streamwise energy spectra for different parameters of the Smagorinsky SGS model compared against the scale-dependant dynamic model.[9] An excellent agreement in the streamwise spectra for our best-performing model ($C_0^{19} n^{05} k_c^{4/7}$) at different length scales with the state-of-the-art LES model[9] for the neutral atmospheric boundary layer is notable. For the more detailed spectral analysis of the models, the variation of streamwise energy spectra at four different heights is shown in Fig. 10. It was observed that the effect of filtering in near wall models was not conspicuous in the spectra, except for, perhaps, a very slight effect at the largest scales of motions. A reference plot in Fig. 11 for the SGS model $C_0 = 0.19$, $n = 0.5$ with different k_c is provided to support the claim above. From hereafter, we would tailor our discussions mostly to the effect of SGS closures since they have more significant impact on the spectral results. Furthermore, it is worth mentioning that the spectral plots in this section and Secs. IV C 2 and IV D are corroborated by a *grid sensitivity* analysis (see Appendix C for details) which illustrates the fact that the scaling laws and the shape of the spectra have a more dominant effect from the wall model LES than the grid itself.

While the case $C_0^{19} n^{05} k_c^{4/7}$ predicts the correct −1 and −5/3 scaling law along with the regime of change of the scaling at $k_x z \sim O(10^0)$, the situation is quite different for "overdissipative" (Cases $C_0^{16} n^2 k_c^{4/7}$, $C_0^{17} n^1 k_c^{4/7}$) as well as "underdissipative" ($C_0^{09} n^2 k_c^{4/7}$) models. For Smagorinsky based overdissipative models, the $k_x^{-5/3}$ law near the wall, $z/H \ll 0.1$, is absent and the location of the k_x^{-1} regime is shifted to larger length scales with a much shorter extent, indicating that the change of scaling laws occurs at $k_x z \sim O(10^{-1})$. The −5/3 law cascade, however, is recovered in the outer layer, $z/H > 0.1$.

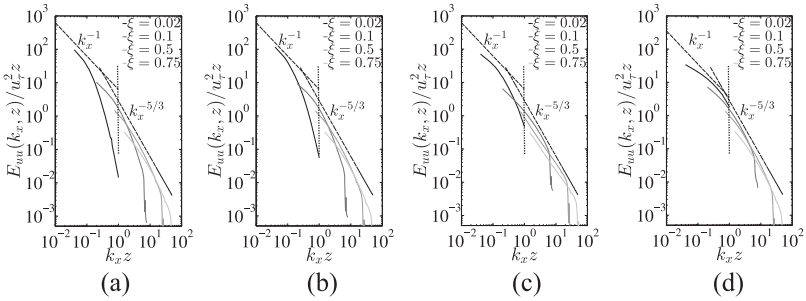

FIG. 10. Normalized streamwise energy spectra $E_{uu}(k_x,z)/u_\tau^2 z$ vs $k_x z$ at different normalized heights $\xi = z/H = 0.02, 0.1, 0.5, 0.75$. (a) Case $C_0^{16} n^2 k_c^{4/7}$, (b) case $C_0^{17} n^1 k_c^{4/7}$, (c) case $C_0^{09} n^2 k_c^{4/7}$, and (d) case $C_0^{19} n^{05} k_c^{4/7}$. Vertical dotted line—$k_x z = 10^0$.

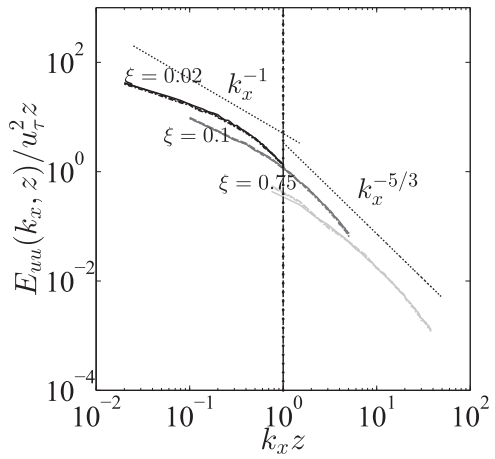

FIG. 11. Normalized streamwise energy spectra $E_{uu}(k_x, z)/u_\tau^2 z$ vs $k_x z$ at different heights $\xi = z/H = 0.02, 0.1, 0.5$ for different values of $k_c/N = 2/7$ (solid line), 4/7 (dashed line), 6/7 (chain dotted line) in explicit filtering of the NWM for models $\{C_0 = 0.19, n = 0.5\}$. Dashed circle—$k_x z = 10^0$

What is surprising is that with "underdissipative effects" as in the case $C_0^{09} n^2 k_c^{4/7}$, the improvement in the spectral scaling near the wall is not noticeable. While the dissipation in the finer scales is indeed smaller, it still cannot recover the −5/3 law and neither does it reflect the correct location of the k_x^{-1} law. The under-dissipative effects are further pronounced at the outer layer, with the scaling law of the power scales clearly deviating from the −5/3 law, manifesting an inefficient cascade. A point of further concern is the region of $k_x^{-1/2}$ scaling which was also observed from the data of the previous literature,[9,75] which is conspicuously absent in all the models, except for the case $C_0^{19} n^2 k_c^{4/7}$.

The fact that the extent and location of length scales of the k_x^{-1} scaling are not captured in some of our LES simulations, e.g., cases $C_0^{16} n^2 k_c^{4/7}, C_0^{09} n^2 k_c^{4/7}, C_0^{17} n^1 k_c^{4/7}$, can be attributed to the effects of "incorrect SGS dissipation" at different distances from the wall, as manifested by the 1D premultiplied streamwise energy spectra contours $k_x E_{uu}(k_x, z)/u_\tau^2$ in Fig. 12. Figures 12(a)–12(c) clearly indicate that only case $C_0^{19} n^{05} k_c^{4/7}$ shows the linear growth of length scales λ_x with distance z from the wall, for a band of energy contours, corresponding to the *logarithmic layer*.[28,39] While case $C_0^{16} n^2 k_c^{4/7}$ retains some of the linear scaling close to $z/H \sim 0.1$, a significant deviation from the linear trend occurs for scales $\lambda_x < H$. Case $C_0^{09} n^2 k_c^{4/7}$ displays, perhaps the worst behavior, with non-linear scaling of λ_x vs z even for the larger scales of motion, $\lambda_x \geq H$.

The discussion above suggests that a proper LES model should provide an optimum amount of dissipation in each region, and simply lowering C_0, while decreasing the near-wall filter scales and improving the near-wall behavior of the spectra, results in *underdissipation* and incorrect scaling law predictions in the outer layer. Control of the SGS dissipation through the change of the shape function in Eqs. (6) and (7) via the two parameters, C_0 and n, which permits a slower growth rate of C_s in the inner layer (case $C_0^{19} n^{05} k_c^{4/7}$), provides an appropriate amount of dissipation for both the inner and the outer layers in the current SEM method.

We plot the shear stress spectra for the parametric variation of wall-damped SGS models at a fixed $k_c/N = 4/7$ (cases $C_0^{16} n^2 k_c^{4/7}, C_0^{09} n^2 k_c^{4/7}, C_0^{17} n^1 k_c^{4/7}, C_0^{19} n^{05} k_c^{4/7}$) in Fig. 13. Similar to the streamwise spectra (Fig. 10), distinct scaling laws also exist in the shear stress spectra. Corresponding to the two overlap regions in the E_{uu} spectra,[33] i.e., k_x^{-1} and $k_x^{-5/3}$

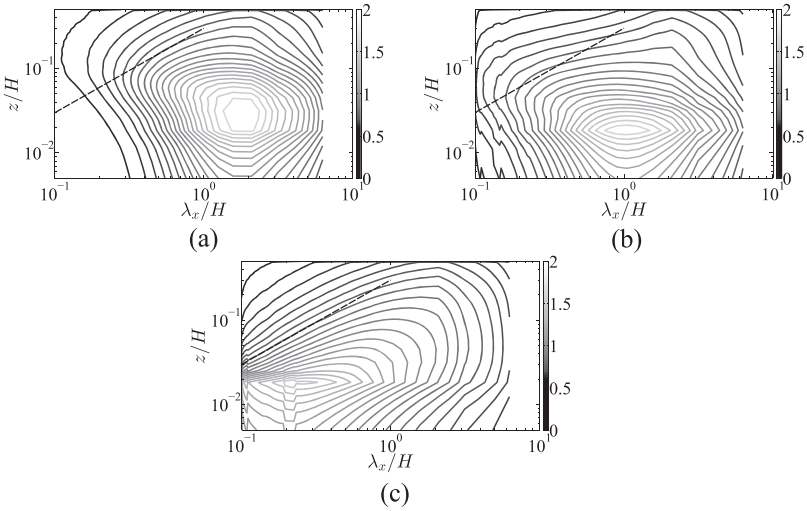

FIG. 12. Premultiplied normalized 1D spectra contour-map $k_x E_{uu}(k_x, z)/u_\tau^2$ for different LES models in the streamwise wavenumber-wall normal distance plane. Streamwise wave number λ_x and wall distance z are both normalized by ABL thickness H. (a) Case $C_0^{16} n^2 k_c^{4/7}$, (b) case $C_0^{09} n^2 k_c^{4/7}$, and (c) case $C_0^{19} n^{05} k_c^{4/7}$. Dashed line: $\lambda_x/H \sim z/H$.

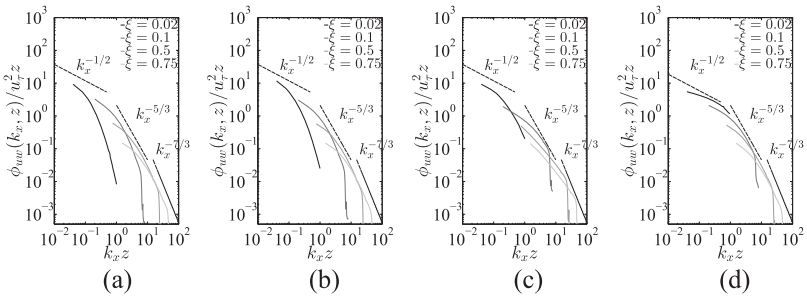

FIG. 13. Normalized shear stress spectra $\phi_{uw}(k_x, z)/u_\tau^2 z$ vs $k_x z$ at different normalized heights $\xi = z/H = 0.02, 0.1, 0.5, 0.75$. (a) Case $C_0^{16} n^2 k_c^{4/7}$, (b) case $C_0^{17} n^1 k_c^{4/7}$, (c) case $C_0^{09} n^2 k_c^{4/7}$, and (d) case $C_0^{19} n^{05} k_c^{4/7}$.

laws, one will also have k_x^0 and $k_x^{-5/3}$ regions in the E_{ww} spectra.[30,33,81] For the near-wall organized motions carrying significant amount of Reynolds stresses, the large- and intermediate-scale organized motions near the wall should be well correlated in terms of u, w motions, i.e., $\phi_{uw}(k_x, z) \approx E_{uu}(k_x, z)^{1/2} E_{ww}(k_x, z)^{1/2}$, where ϕ_{uw} is the spectra of the kinematic shear stress $-\overline{u'w'}$.[30] Correspondingly, the scaling laws of the two overlap regions of the cospectra, $\phi_{uw}(k_x, z)$, would be $k_x^{-1/2}$ and $k_x^{-5/3}$ laws, respectively, with smaller scales in the far-outer region depicting the classical $k_x^{-7/3}$ law.[81–83]

We observe that only for the case $C_0^{19} n^{05} k_c^{4/7}$, we can capture the theoretical scaling laws of the shear stress spectra in the inner and outer wall regions. Case $C_0^{09} n^2 k_c^{4/7}$, even though retains the $k_x^{-1/2}$ and $k_x^{-5/3}$ laws in the near wall region, depicts strong deviation from the $k_x^{-5/3}$, $k_x^{-7/3}$ scaling laws in the outer layer. However, the overdissipative models, cases $C_0^{16} n^2 k_c^{4/7}$ and $C_0^{17} n^1 k_c^{4/7}$, cannot even predict the first overlap region, illustrating an incorrect slope of what seems to be closer to $k_x^{-3/4}$ rather than the expected $k_x^{-1/2}$, even though the intermediate/small scale laws, $k_x^{-5/3}$, $k_x^{-7/3}$, are captured quite well. This incorrect $k_x^{-3/4}$ scaling will be elaborated upon further in Sec. IV C 2. Additionally, in all models except for the case $C_0^{19} n^{05} k_c^{4/7}$, the normalized streamwise energy spectra and cospectra at different heights do not collapse well in the overlap regions specifying that they do not scale well with $u_\tau^2 z$ specifically in the near-wall region.

2. Near wall correlations

To understand the counter-intuitive behavior of the dissipative Smagorinsky models in affecting the larger length scales of the Reynolds stresses [manifested by the fact that models $C_0^{16} n^2 k_c^{4/7}$, $C_0^{17} n^2 k_c^{4/7}$ predict a $k_x^{-3/4}$ scaling law instead of a $k_x^{-1/2}$ law of the shear stress spectra as seen in Figs. 13(a) and 13(c)], we try to investigate how the u, w wall correlations of the near-wall organized structures are affected by the parametric variation of SGS models. The plots of $E_{uu}, E_{ww}, \phi_{uw}$ at two different normalized heights $\xi = 0.02, 0.025$ for the cases $C_0^{16} n^2 k_c^{4/7}$, $C_0^{09} n^2 k_c^{4/7}$, $N_\sigma k_c^{4/7}$, $C_0^{19} n^{05} k_c^{4/7}$ are shown in Fig. 14. It was observed that well *correlated* scaling laws in the near wall corresponding to $\phi_{uw} \approx E_{uu}^{1/2} E_{ww}^{1/2}$ exist only for the models $C_0^{16} n^2 k_c^{4/7}$, $C_0^{17} n^1 k_c^{4/7}$, $C_0^{19} n^{05} k_c^{4/7}$. For the correlated regions in the overlap, if $E_{uu} \sim A_1 u_\tau^2 k_x^{-l}$, $E_{ww} \sim A_3 u_\tau^2 k_x^{-m}$, and $\phi_{uw} \sim A_{13} u_\tau^2 k_x^{-n}$, one would require $n = (l + m)/2$.[33]

We list the observed scaling laws for E_{uu}, E_{ww}, and ϕ_{uw} for the first overlap region (corresponding to a k_x^{-1} region of the streamwise spectra) for the models $C_0^{16} n^2 k_c^{4/7}$, $C_0^{09} n^2 k_c^{4/7}$, $C_0^{17} n^1 k_c^{4/7}$, $N_\sigma k_c^{4/7}$, and $C_0^{19} n^{05} k_c^{4/7}$, together with the correlation coefficient $\rho_{uw} = A_{13}/(\sqrt{A_1}\sqrt{A_3})$, in Table III. The correlation coefficient is expected to be high for well correlated models. Table III confirms that the models $C_0^{16} n^2 k_c^{4/7}$, $C_0^{17} n^1 k_c^{4/7}$, and $C_0^{19} n^{05} k_c^{4/7}$ depict the presence of the near-wall correlation, with the value of the correlation coefficient roughly at ~ 83%. Although the models $C_0^{16} n^2 k_c^{4/7}$ and $C_0^{17} n^1 k_c^{4/7}$ do reveal the wall correlation, the scaling laws for the co-spectra are incorrect, which, as can be seen from Fig. 14(a) and Table III, comes from the incorrect E_{ww} spectra. It is the model $C_0^{19} n^{05} k_c^{4/7}$ that not only produces the near-wall correlations but also gives the correct scaling laws for the correlations. Interestingly, for the model $C_0^{09} n^2 k_c^{4/7}$, although it produces the correct scaling for the co-spectra, the near-wall correlation does not exist due to, again, a wrong scaling of the w component.[24]

Table III also lists the range of $k_x z$ values where the scalings characteristic to the region were observed. Note that it is $k_x z < 10^{-1}$ for the three models $C_0^{16} n^2 k_c^{4/7}$, $C_0^{17} n^1 k_c^{4/7}$, $C_0^{19} n^{05} k_c^{4/7}$ and $10^{-1} < k_x z < 10^0$ for the model $C_0^{19} n^{05} k_c^{4/7}$.

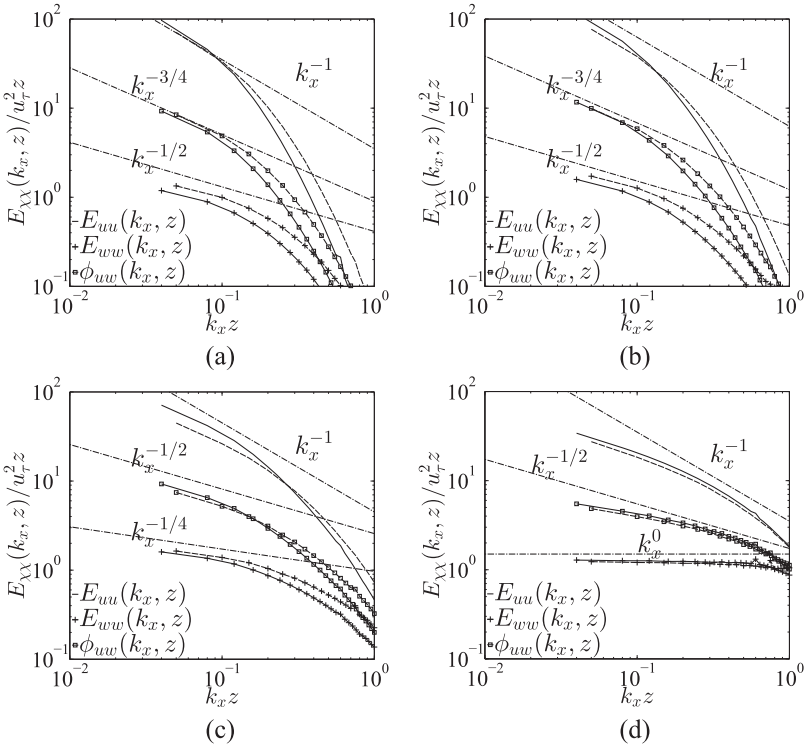

FIG. 14. Near wall u, w spectral correlation scale comparing $E_{\chi\chi}(k_x, z) = E_{uu}(k_x, z), E_{ww}(k_x, z), \phi_{uw}(k_x, z)$ all normalized with $u_\tau^2 z$ at normalized wall distance $\xi = 0.02, 0.025$. (a) Case $C_0^{16} n^2 k_c^{4/7}$, (b) case $C_0^{17} n_\sigma^1 k_c^{4/7}$, (c) case $C_0^{09} n^2 k_c^{4/7}$, and (d) case $C_0^{19} n^{05} k_c^{4/7}$. Solid line—$z/H = 0.02$; dashed line—$z/H = 0.025$.

TABLE III. Near wall u, w scaling laws, their correlation coefficient in the first overlap region (k_x^{-1} region of E_{uu} spectra), and wavenumber range for four different parametric variations of the wall-damped SGS model $C_0^{16}n^2k_c^{4/7}$, $C_0^{17}n^1k_c^{4/7}$, $C_0^{09}n^2k_c^{4/7}$, and $C_0^{19}n^{05}k_c^{4/7}$.

Case	E_{uu} scaling	E_{ww} scaling	ϕ_{uw} scaling	Observed k_xz range	$\rho_{uw} = A_{13}/\sqrt{A_1}\sqrt{A_3}$
$C_0^{16}n^2k_c^{4/7}$	k_x^{-1}	$k_x^{-1/2}$	$k_x^{-3/4}$	$k_xz < 10^{-1}$	0.8243
$C_0^{17}n^1k_c^{4/7}$	k_x^{-1}	$k_x^{-1/2}$	$k_x^{-3/4}$	$k_xz < 10^{-1}$	0.825
$C_0^{09}n^2k_c^{4/7}$	k_x^{-1}	$k_x^{-1/4}$	$k_x^{-1/2}$	$k_xz < 10^{-1}$	...
$C_0^{19}n^{05}k_c^{4/7}$	k_x^{-1}	k_x^{0}	$k_x^{-1/2}$	$10^{-1} < k_xz < 10^{0}$	0.8333

The correlations that we see in the near-wall spectra are associated with the attached inactive motions as discussed in Sec. IV C. The case $C_0^{19}n^{05}k_c^{4/7}$ predicts the correct upperbound of the *active wall normal motions*, $k_xz \sim 10^0$, corresponding to $\lambda_x/z \sim O(10^1)$, while the other three cases $C_0^{16}n^2k_c^{4/7}$, $C_0^{09}n^2k_c^{4/7}$, $C_0^{17}n^1k_c^{4/7}$ overpredict the size of these active motions by a decade, $k_xz \sim 10^{-1}$, or $\lambda_x/z \sim O(10^2)$, in addition to producing an incorrect scaling in cases $C_0^{16}n^2k_c^{4/7}$, $C_0^{17}n^1k_c^{4/7}$ and uncorrelated u, w motions in the case $C_0^{09}n^2k_c^{4/7}$. We must mention that the case $C_0^{19}n^{05}k_c^{4/7}$ predicts the $E_{uu} \sim k_x^{-1/2}$ scaling for such large-scale eddies, $k_xz \sim 10^{-1}$, $\lambda_x/z \sim O(10^2)$, see Table IV, consistent with the previous observations at high Reynolds numbers,[9,75] which are also well correlated, with the same correlation coefficient of ~83% as the k_x^{-1} law. As discussed in Sec. IV C, we surmise that the −1/2 scaling law might possibly be a modification to the k_x^{-1} scaling with certain correction factors as predicted in Ref. 30, but also caution the readers that careful analysis needs to be performed at larger computational domains before we can conjecture on the possible implication of the −1/2 region.[31]

D. 2D spectra

While the analysis of 1D spectra depicts the inner and outer layer streamwise length scales of the eddies affected by SGS dissipation, they cannot predict the structure of the eddies being influenced by the LES dissipation. The potential of 2D spectra in identifying eddy structures has been long realized since the last two decades in simulations[30–32,84] and experiments.[28,29,70,85] In the above studies, 2D spectra have been utilized to estimate the streamwise and spanwise length scales of the near wall eddies consistent with Townsend's attached eddy hypothesis[4] in wall bounded turbulence.

Figure 15 shows the 2D premultiplied streamwise energy spectra, $k_xk_yE_{uu}(k_x, k_y, z)$, in the plane of streamwise-spanwise wavelengths for different SGS models as in cases $C_0^{16}n^2k_c^{4/7}$, $C_0^{09}n^2k_c^{4/7}$, $C_0^{19}n^{05}k_c^{4/7}$. Similar to the 1D spectra, the effect of explicit filtering has been found to be inconsequential to the analysis of active and inactive length scales and their scaling laws and has been omitted from discussion from here onwards. We compare the spectral results with $k_c = 4/7$ since this value of cutoff together with our model case $C_0^{19}n^{05}k_c^{4/7}$ gives the best results for the log-law of the wall.

1. Inner layer

The theoretical scaling laws of λ_x, λ_y in the inner layer ($\xi < 0.1$) can be only observed in case $C_0^{19}n^{05}k_c^{4/7}$ with the *active motions* corresponding to $\lambda_y \sim \lambda_x$ extending from the minimum resolved length scale to $\lambda_x \sim 10z$ at the spectral ridge, beyond which the *attached inactive motions* initiate with the power law scaling [see the schematic in Fig. 7(b) in Sec. IV C for details], as can be judged from Fig. 15(d).

For overdissipative cases like $C_0^{16}n^2k_c^{4/7}$, Figs. 15(a) and 15(c), or underdissipative cases like $C_0^{09}n^2k_c^{4/7}$, Fig. 15(b), the near-wall dynamics are heavily influenced. For the case $C_0^{16}n^2k_c^{4/7}$, the linear scaling $\lambda_y \sim \lambda_x$ of the active motions persists for scales $\lambda_x \sim 100z$, and the power law "***A***" scaling corresponding to $p = 3$ (attached inactive motions) is completely absent. However, traces of 1/3 law "***B***" scaling can still be found for cases $C_0^{16}n^2k_c^{4/7}$, $C_0^{17}n^1k_c^{4/7}$. It is suspected that the absence of a conspicuous inactive eddy region is responsible for the smaller regime of k_x^{-1} in the 1D u spectra [see Fig. 10(a)] which also occurs at larger length scales than anticipated. For the case $C_0^{09}n^2k_c^{4/7}$, however, even though the scaling corresponding to the *active motions* is present at $\lambda_x < 10z$, none of the power-law "***A***," "***B***" ($p = 3$) scalings corresponding to the *inactive motions* can be conspicuously identified in the near wall region.

2. Outer layer

However, at the outer-layer ($\xi > 0.1$), the models $C_0^{16}n^2k_c^{4/7}$, $C_0^{19}n^{05}k_c^{4/7}$ predict the square-root scaling, $\lambda_y/z \sim (\lambda_x/z)^{1/2}$ corresponding to the longer-narrower structures ($\lambda_x > \lambda_y$). The square-root scaling analysis in the outer layer would be similar to that of the inner layer, mainly due to similar dynamics of long term dispersion of background turbulence (see Refs. 30 and 31 for details). This is, however, not the case

TABLE IV. Near wall u, w scaling laws, their correlation coefficient for the large-scale motions ($k_x^{-1/2}$ region of E_{uu} spectra), and wavenumber range for the case $C_0^{19}n^{05}k_c^{4/7}$.

Case	E_{uu} scaling	E_{ww} scaling	ϕ_{uw} scaling	Observed k_xz range	$\rho_{uw} = A_{13}/\sqrt{A_1}\sqrt{A_3}$
$C_0^{19}n^{05}k_c^{4/7}$	$k_x^{-1/2}$	k_x^{0}	$k_x^{-1/4}$	$k_xz < 10^{-1}$	0.8365

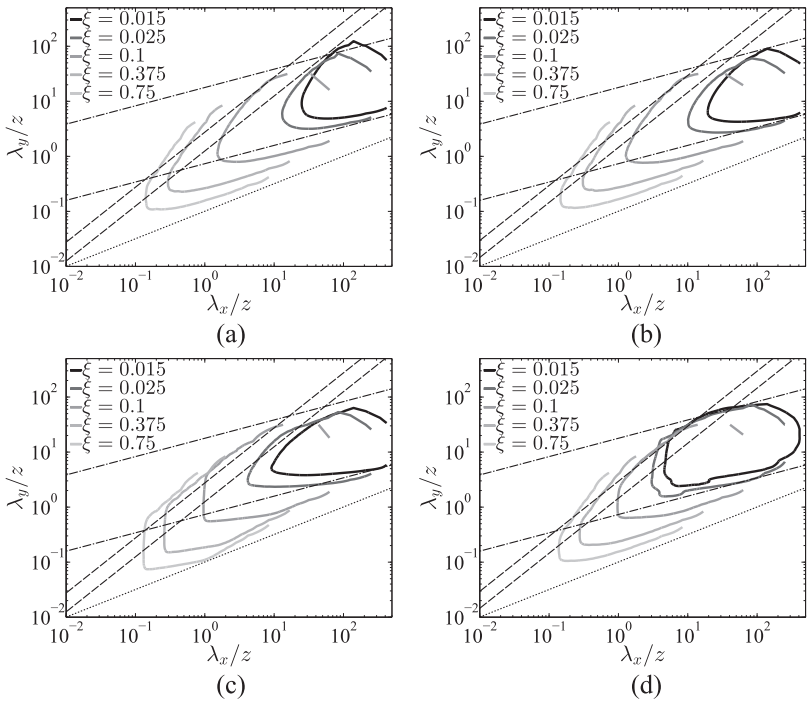

FIG. 15. Premultiplied 2D streamwise energy spectra $k_x k_y E_{uu}(k_x, k_y)$ in the streamwise-spanwise wave number plane, λ_x/z and λ_y/z, normalized with inertial length scale z, $\lambda_{x,y} = 2\pi/(k_{x,y})$. (a) Case $C_0^{16} n^2 k_c^{4/7}$, (b) case $C_0^{17} n_\sigma^1 k_c^{4/7}$, (c) case $C_0^{09} n^2 k_c^{4/7}$, and (d) case $C_0^{19} n^{05} k_c^{4/7}$. All plots are at 5 different heights $\xi = z/H = 0.015$, 0.025, 0.1, 0.375, 0.5, with lighter line color shades with increasing ξ. All contours are at 0.125 times of maximum. Dashed black line—$\lambda_y/z \sim \lambda_x/z$; dotted black line—$\lambda_y/z \sim (\lambda_x/z)^{1/2}$; chain dotted black line—$\lambda_y/z \sim (\lambda_x/z)^{1/3}$.

for the model $C_0^{09} n^2 k_c^{4/7}$, where no such square root scaling is distinctly identified, as we move into the far-outer layer. It is perhaps not hard to associate this absence of the square root scaling in the outer-layer with the absence of a proper −5/3 law cascade of the 1D spectra, all indicating towards the underdissipative effects.

In order to understand the implications of the presence or absence of the scaling laws as described above, we also plot all the u, v, w energy and $\overline{u'w'}$ shear-stress spectra at $z/H = 0.15$ in Figs. 16(a)–16(c), obtaining qualitatively similar structures as in Ref. 39 [reproduced here in Fig. 16(d)]. While the case $C_0^{19} n^{05} k_c^{4/7}$ displays a qualitatively similar picture with the DNS of the channel flow simulations in Ref. 39, with some minor discrepancies arising due to a difference in the domain size, the situation is quite different for cases $C_0^{16} n^2 k_c^{4/7}$, $C_0^{09} n^2 k_c^{4/7}$. Due to the overdissipative effects of the case $C_0^{16} n^2 k_c^{4/7}$, for scales $\lambda_x > 10z$, the linear scaling persists for the u spectra, and also w spectra erroneously extends to these large scales, implying that the 3D active turbulent motions become artificially large for case $C_0^{16} n^2 k_c^{4/7}$, extending to scales where the two dimensional inactive motions should have been present. For the underdissipative case of $C_0^{09} n^2 k_c^{4/7}$, the scale $\lambda_x \sim 10z$ corresponds to the long-wavelength cutoff for the w spectra, which is physically consistent from the perspective of the size of the active motions. The 1/3 scaling law, however, is absent.

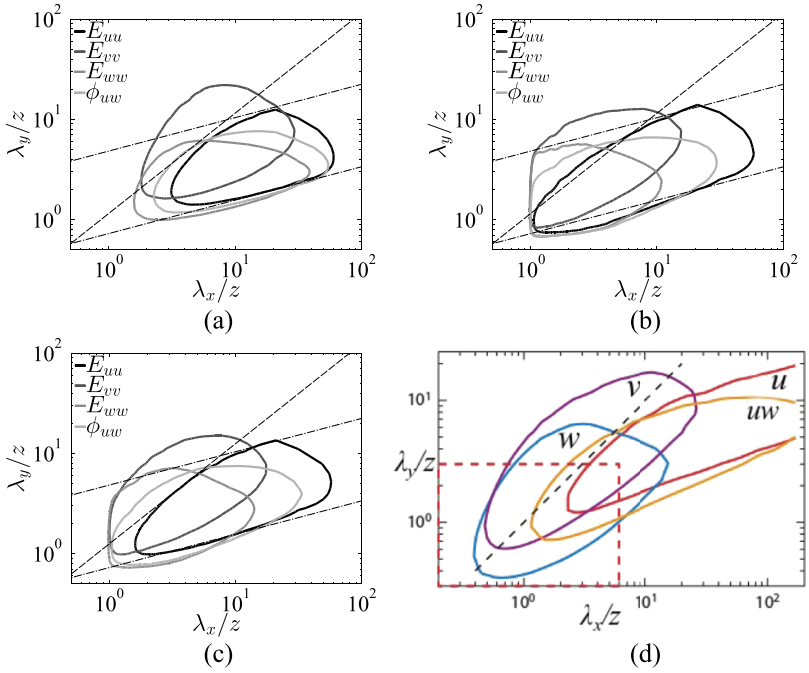

FIG. 16. [(a)–(d)] Premultiplied 2D streamwise energy spectra $k_x k_y E_{\xi\xi}(k_x, k_y, z)$ ($\xi = u, v, w$) and cospectra $k_x k_y \phi_{uw}(k_x, k_y)$ in the streamwise-spanwise wave number plane at $z/H = 0.15$. (a) Case $C_0^{16} n^2 k_c^{4/7}$, (b) case $C_0^{09} n^2 k_c^{4/7}$, and (c) case $C_0^{19} n^{05} k_c^{4/7}$. Premultiplied spectra of E_{uu}, E_{vv}, E_{ww}, and ϕ_{uw} are plotted in progressively lighter shades of gray. The contours in (a)–(d) are at 0.4 times of their maximum. Dashed black line—$\lambda_y/z \sim \lambda_x/z$; chain dotted black line—$\lambda_y/z(\lambda_x/z)^{1/3}$. (e) Premultiplied 2D energy spectra and cospectra of channel flow taken from the work of Jiménez[39] reproduced with permission from J. Jiménez, Annu. Rev. Fluid Mech. **44**, 27–45 (2012). Copyright 2012 Annual Reviews. http://www.annualreviews.org.

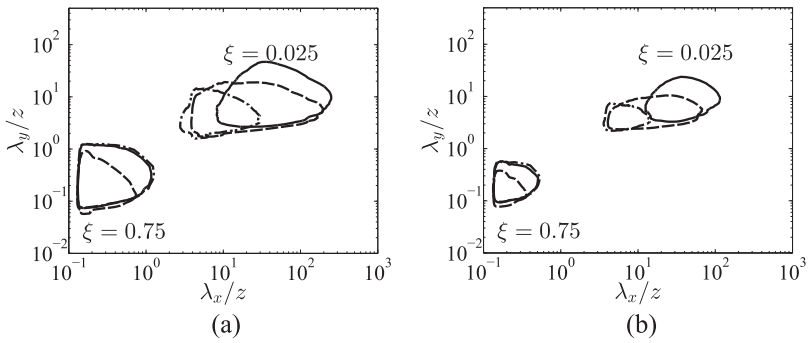

FIG. 17. Premultiplied enstrophy spectra $k_x k_y E_{\omega\omega}(k_x, k_y, z)$ in the streamwise-spanwise wavenumber plane for different cases $C_0^{16} n^2 k_c^{4/7}$, $C_0^{09} n^2 k_c^{4/7}$, $C_0^{19} n^{05} k_c^{4/7}$. (a) Contour level of 25% of the maximum. (b) Contour level of 50% of the maximum. $\xi = z/H$ is the normalized distance from the wall. Solid line—case $C_0^{16} n^2 k_c^{4/7}$, dashed line—case $C_0^{09} n^2 k_c^{4/7}$, chain dotted line—case $C_0^{19} n^{05} k_c^{4/7}$.

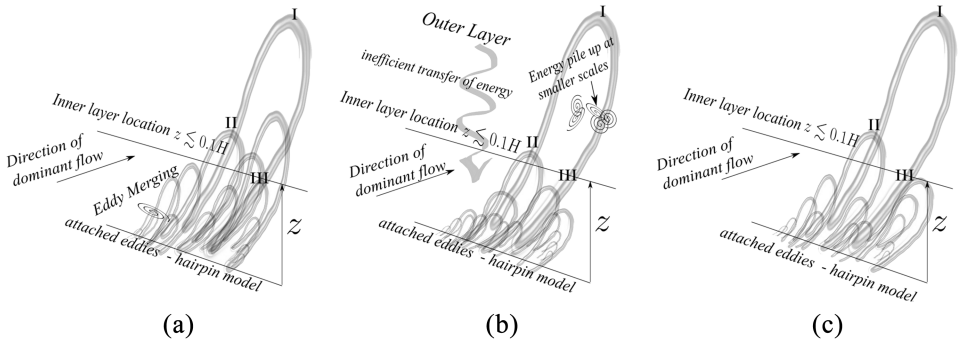

FIG. 18. Sketch (not to scale) of the near wall dynamics for (a) overdissipative ($C_0 = 0.16$, $n = 2$), (b) underdissipative ($C_0 = 0.09$, $n = 2$), and (c) optimally dissipative ($C_0 = 0.19$, $n = 0.5$) wall-damped Smagorinsky SGS models. Attached eddies are illustrated using *hairpin vortices*. I, II, and III are the representative eddies at different wall locations.

The above observations are the indication of a requirement of an *optimal* SGS dissipation in our spectral-element LES models, which can be further illustrated if we look into the 2D premultiplied enstrophy spectra ($k_x k_y E_{\omega\omega} = k_x k_y \langle \hat{\omega}\hat{\omega}^* \rangle$, where $\hat{\omega}$ is the Fourier transform of vorticity) in Figs. 17(a) and 17(b). Enstrophy is often considered as a surrogate for the turbulent dissipation,[84,86,87] and in our case, it is a good representative of the total (i.e., Kolmogorov + SGS) dissipation in the LES models. For cases $C_0^{09} n^2 k_c^{4/7}$, $C_0^{19} n^{05} k_c^{4/7}$, the smallest scales of motion in the near-wall dissipation ($\xi = z/H = 0.025$) are $\lambda_x < 10z$. In the case $C_0^{16} n^2 k_c^{4/7}$, a severe near-wall dissipation hinders the growth of small scale dissipative eddies, and the smallest resolved scales are $\lambda_x \gtrsim 10z$ that correspond to the range of attached inactive motions. In the outer layer ($\xi = z/H = 0.75$), the dissipation characteristics for cases $C_0^{16} n^2 k_c^{4/7}$, $C_0^{19} n^{05} k_c^{4/7}$ collapse, confirming the correct −5/3 cascade seen in Figs. 10(a), 10(c), and 10(d), while for the case $C_0^{09} n^2 k_c^{4/7}$ [Fig. 10(b)], the largest scales involved in the outer-layer dissipation are much smaller than in the cases $C_0^{16} n^2 k_c^{4/7}$, $C_0^{19} n^{05} k_c^{4/7}$, revealing an inefficient cascade.

In general, before we conclude, a brief summary of the behavior of the wall-damped Smagorinsky based SGS models with different parameters is presented in this paragraph. Figure 18 is a qualitative sketch (picture not to scale) of the attached eddies (hairpin vortices attached to the "wall" at an acute angle ~10°) obtained from the spectral information as discussed above. The representative hairpin-like eddy I is of length scale $\lambda_x \gg 10z$, and hence at the height of z, it would essentially represent a horizontal two-component u, v flow[33] corresponding to attached *inactive motions*. Eddies of scale $\lambda_x \sim O(z)$ (representative eddies II, III) are responsible for the 3D *active motions*. For an overdissipative model, the eddy viscosity results in the mixing of the eddies near the wall and attenuation of the small scale phenomenon. This inflicts an artificial abundance of the *active* eddies of the $O(z)$ scale, and hence the 3D motions (averaged over all eddies) extend to longer scales as seen in Fig. 16(a), which is schematically

TABLE V. A summary of the behavior of different SGS models $C_0^{16} n^2 k_c^{4/7}$, $C_0^{17} n^1 k_c^{4/7}$, $C_0^{09} n^2 k_c^{4/7}$, $C_0^{19} n^{05} k_c^{4/7}$ compared against 9 important trends in physical and spectral domains that represent inner and outer layer physics. (i) LLM—Log Layer Mismatch, (ii) TS trends—scaling trends in the vertical variation of turbulent stresses near the wall at $z/H < 0.1$, (iii) $k_x^{-1/2}$ scaling of the streamwise spectra near wall, (iv) k_x^0 scaling of the wall-normal spectra near the wall, (v) $\lambda_y \sim \lambda_x^{1/2}$ scaling of premultiplied 2D streamwise spectra at the outer layer, (vi) $k_x^{-5/3}$ scaling of the velocity spectra and cospectra at the outer layer, (vii) SR location—location of the spectral ridge where linear to power law scaling transition occurs for premultiplied 2D streamwise spectra, serving as a barrier between active and inactive motions.

LES models	LLM	TS trends	$E_{uu} \sim k_x^{-1/2}$	$E_{ww} \sim k_x^0$	$\lambda_y \sim \lambda_x^{1/2}$	−5/3 scaling	SR location
$C_0^{16} n^2 k_c^{4/7}$	Yes	Incorrect	No	No	Yes	Yes	Incorrect
$C_0^{17} n^1 k_c^{4/7}$	Yes	Incorrect	No	No	Yes	Yes	Incorrect
$C_0^{09} n^2 k_c^{4/7}$	Yes	Incorrect	No	No	No	No	Incorrect
$C_0^{19} n^{05} k_c^{4/7}$	No	Correct	Yes	Yes	Yes	Yes	Correct

illustrated in Fig. 18(a). This also weakens the vertical near-wall motions (w) manifested by the attenuation of $\widetilde{w'^2}$ in Fig. 6. An underdissipative case [Fig. 18(b)] actually allows for much smaller eddies near the wall to be sustained, but an inefficient forward energy cascade in the outer layer [see Fig. 10(c)] results in a pileup of energy at smaller length scales. For the optimally dissipative case [Fig. 18(c)], the size of the near wall eddies represents the correct distribution of the length scales of the near-wall eddies[33] which eliminates the presence of "artificial viscous sublayer," in concordance with Townsend's attached eddy hypothesis.[4] Table V further summarizes the scaling laws and the observed correct or incorrect physics of the inner and outer layer eddies with the different parameters of the Smagorinsky-based SGS models.

V. CONCLUSION AND FUTURE WORK

The current studies involving the different LES models not only provide the design procedure for the reliable yet inexpensive SGS models in the spectral element framework but also focus on another important aspect—the behavior of the eddies in wall-turbulence, under the influence of artificial length scales introduced by Smagorinsky based subgrid-scale eddy viscosity closures.

We found that the LES results are extremely sensitive to the parameters of the subgrid-scale closure model, and the Smagorinsky based SGS models need to be "optimally tuned" to retrieve the correct flow physics. Our results have been further strengthened by the grid sensitivity analysis (Appendix C) which also manifests the robustness of the proposed LES models designed in the spectral element framework. It has been observed that the elimination of the effect of artificial SGS filtering length scales in our LES model is possible by reducing the growth rate of the filter scale l_f near the wall by reducing n while simultaneously increasing C_0 slightly, to a threshold, beyond which the physical length scales become dominant, which helps produce the correct turbulent statistics and spectra. The results, on the other hand, are not significantly affected by the explicit filtering in the near-wall modeling, except, perhaps, the amount of log layer mismatch and the spectra in the largest scales of motions near the wall. The exact reason is still not entirely understood and requires further investigation, but it can be attributed to the amount of removal of the near-wall dissipative scales through filtering. Based on our computations, the model $C_0^{19}n^{05}k_c^{4/7}$ is advocated to be the best model used for LES in a spectral element framework.

Investigating the physics of the "artificial length scales" of the different LES models helps build the fundamental understanding of the *inner* and *outer* layer eddies as well as the effect of the SGS closure on the formation of "eddy viscosity" sub-layer. The principal findings in the current work are summarized below, by the following points:

(i) Apart from influencing the fine-scale dissipative eddies and the energy cascade (−5/3 law) near wall, the Smagorinsky based SGS models are also found to affect the larger scales as well, e.g., the active and inactive motions.

(ii) Overdissipation of the Smagorinsky SGS models affects the length scales of the *3D active motions* in the inner layer, making them as large as the *2D inactive* ones possibly due to "mixing of eddies." The absence of conspicuous regions of inactive motions can be correlated with a smaller, erroneous, regime of the k_x^{-1} law.

(iii) Underdissipation of SGS models results in the larger scales of motion at the outer layer not loosing enough energy through the transfer mechanism (SGS dissipation). This is supposedly reflected in the incorrect scaling and hence dynamics of the *attached inactive motions* near the wall, supporting the fact that the outer-layer motions also influence the near-wall structures.

(iv) Both the effects of over- and under-dissipation in Smagorinsky based models detrimentally influence the near-wall organization, more severely through the vertical energy, or w spectra, resulting in incorrect u, w correlations near the wall. For over-dissipation, the effect of incorrect w spectra is also seen in extending the length scales of 3*D* active motions.

(v) In the outer layer, the correct prediction of −5/3 scaling law as seen in the u spectra is inherently related to capturing the square-root scaling of 2D u spectra corresponding to dispersion of eddies in background turbulence.

These outcomes indicate that "optimum LES dissipation," both in the inner and the outer layers, is required for correctly resolving the large-scale flow physics in neutral ABL flows. Consequently, it is reasonable to conclude that the log-law of the wall, the location of k_x^{-1} law, and the scaling of the active and inactive motions near the wall are closely associated with the proper SGS dissipation in every region of the flow. From a practical viewpoint, our study shows that the "optimal dissipation" can still be obtained from a fine-tuned standard wall-damped Smagorinsky model, without having to use more expensive dynamic models. We believe that the present static model is not limited to neutral atmospheric boundary layer flow simulations but can be further extended to flows with variable aerodynamic roughness, flows past wind turbine arrays,[48,56] and potentially generalized to atmospheric flows with varying atmospheric conditions, including stable and unstable stratification invoking Monin-Obukov similarity.[3,15]

The present paper not only provides design criteria for LES-NWM models in wall bounded turbulence from the perspective of fundamental physics but also opens up a plethora of research possibilities for studying the eddy structures in wall-bounded turbulence, using the LES model. In a spectral element framework, where the discretization errors are inherently small, the SGS closure and the near-wall modeling are the two approximations that determine, to a large extent, the impact of artificiality on the numerical results. As a future work, this well-controlled "artificial laboratory" framework provides an opportunity to study the flow in a larger computational domain and analyze if certain large structures in the inner and outer layers can be sustained in isolation, without the presence of other structures. The Smagorinsky

model, as well as other static dissipative models like Vreman,[88] WALE,[89] or Sigma[90] model, can be specifically used to induce "user-controlled" artificial dissipation in "shear-dominated" or "rotation-dominated" regions masking out certain regions or certain eddies in the flow. This radical approach would help provide further insights into the physics of large scale structures (LSM's, VLSM's) in high *Re* wall-turbulence, which are still relatively poorly understood unlike the mean statistics in turbulence. Studies of wall-bounded turbulence along the similar lines have been initiated by Jiménez *et al.*,[30,91] who masked out certain regions of the DNS flow, or by Hwang[32] and Rawat *et al.*,[92] who used the wall-resolved LES for quenching smaller scales of motion, but all these studies were limited to low and moderate Reynolds numbers. A significant challenge lies in extending these ideas to much larger *Re*, as in ABL turbulence, and to moderately complex geometries. The proposed spectral-element LES methodology in conjunction with near-wall modeling can become a useful tool in realizing this challenge.

ACKNOWLEDGMENTS

The authors T. Chatterjee and Y. Peet would like to gratefully acknowledge the support of NSF-CBET 13358568 grant and computational time on Stampede Supercomputer from XSEDE allocation TG-ENG150019 for the present work. The authors would also like to thank Dr. Paul F. Fischer of Argonne National Laboratory for valuable discussions in spectral element methods.

APPENDIX A: ELEMENTAL LEVEL FILTERING

For the explicit filtering approach in near-wall modeling, we use the modal approach of Boyd,[93] see also Refs. 52 and 53. With the modal filtering technique, decomposition of the variable u into the modal basis is sought,

$$u(\xi_i) = \sum_{k=0}^{N} \hat{u}_k \phi_k(\xi_i), \tag{A1}$$

where $\xi_i, i = 0, \ldots, N$ represent the Gauss-Lobatto-Legendre (GLL)[43] clustering of the nodes inside each element, and the modal basis $\{\phi\}$,

$$\phi_0 = L_0(\xi), \quad \phi_1 = L_1(\xi) \quad \text{and} \quad \phi_k = L_k(\xi) - L_{k-2}(\xi), \quad 2 \le k \le N, \tag{A2}$$

forms the hierarchical set of functions constructed from the Legendre polynomials $L_k(\xi)$. The bubble functions ϕ_k are designed to preserve the homogeneous Dirichlet boundary conditions since $\phi_k(\pm 1) = 0$ for $k \ge 2$ (refer to Ref. 93). The inhomogeneous Dirichlet boundary conditions are satisfied by the low order polynomials ϕ_0, ϕ_1. The mapping between the nodal Lagrangian basis and the modal representation, defined by Eq. (A1), can be cast into the matrix form

$$\mathbf{u} = \Phi \hat{\mathbf{u}}. \tag{A3}$$

Low-pass filtering is performed in the modal space through a diagonal matrix $\mathbb{T}$ whose components are $T_0 = T_1 = 1$ (satisfying C_0 inter-element continuity) and $T_k = f(k; \bar{k}) = 1/(1+(k/\bar{k})^{\gamma})$, $2 \le k \le N$. The function $f(k; \bar{k})$ is an attenuation function and $\bar{k}$ is the threshold value such that $T_k|_{k=\bar{k}} = 1/2$ (see Fig. 19). Parameters $\bar{k}$ and γ determine the precise shape of the filter transfer function. Decreasing $\bar{k}$ attenuates the large scale contents of the filtered velocity $\widetilde{u}_i$, while decreasing γ smoothens the transfer function more towards a non-projective filtering as seen in Figs. 19(a)–19(c). The filtering process in one dimension is given by

$$\widetilde{\mathbf{u}} = \mathcal{G} * \mathbf{u} = \Phi \mathbb{T} \Phi^{-1} \mathbf{u}. \tag{A4}$$

Extrapolation to a 3D field can be achieved from 1D filter by a fast tensor product application.[94] In the current calculations, we define $k_c = N - \bar{k}$ as the number of modes being cut-off and use $\gamma = 12$ (sharp spectral filter).

APPENDIX B: STRESS BOUNDARY CONDITIONS IN WEAK FORMULATION

The viscous term in the weak form of the Navier-Stokes equations can be expanded using an integration by parts as follows:

$$\begin{aligned}\left(\nu \nabla^2 \mathbf{u}, \mathbf{v}\right) &= \left(2\nu \nabla \cdot \nabla^s \mathbf{u}, \mathbf{v}\right) = 2\nu \int_{\Omega} \nabla \cdot \nabla^s \mathbf{u} \cdot \mathbf{v} \mathrm{d}^3\mathbf{x} \\ &= -2\nu \int_{\Omega} \nabla^s \mathbf{u} \cdot \nabla^s \mathbf{v} \mathrm{d}^3\mathbf{x} + \int_{\Omega} 2\nu \nabla \left(\nabla^s \mathbf{u} \cdot \mathbf{v}\right) \mathrm{d}^3\mathbf{x},\end{aligned} \tag{B1}$$

where $\mathbf{u}$ is the velocity vector and $\mathbf{v}$ is a vector in the test space used for Galerkin projection. Here, ∇^s is the symmetric part of the gradient tensor given as $\frac{1}{2}\left(\nabla() + \nabla()^T\right)$, and fluid stress in Ω is $\sigma_{ij} - \frac{1}{3}\sigma_{kk}\delta_{ij} = -2\nu\nabla^s\mathbf{u}$ (Newton's linear stress-strain rate relation). In the derivation of Eq. (B1), we have used the fact that from the divergence constraint $\nabla \cdot \mathbf{u} = 0$, one has

$$\nabla^2 \mathbf{u} = 2\nabla\nabla^s \mathbf{u}.$$

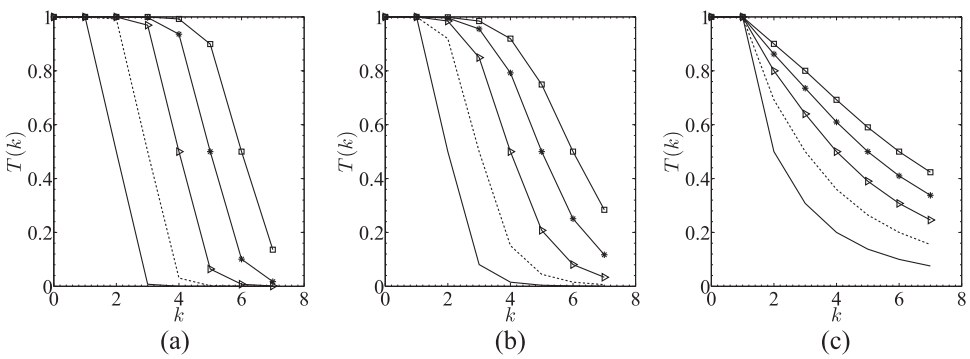

FIG. 19. Filter transfer function $T(k) = (1 + (k/\bar{k})^{\gamma})^{-1}$. (a) $\gamma = 12$, (b) $\gamma = 6$, and (c) $\gamma = 2$. –, $\bar{k} = 2$; – –, $\bar{k} = 3$; –·–△, $\bar{k} = 4$; –⋆, $\bar{k} = 5$; –□, $\bar{k} = 6$ | $T(\bar{k}) = \frac{1}{2}$. The total number of modes $k_{max} = N = 7$, corresponding to GLL nodes = 8 (used in our simulation).

From the Gauss divergence theorem, volume integral in Ω can be replaced by a surface integral in $\partial\Omega$,

$$\int_\Omega 2\nu\,\nabla\left(\nabla^s\mathbf{u}\cdot\mathbf{v}\right)\mathrm{d}^3\mathbf{x} = \oint_{\partial\Omega} 2\nu\nabla^s\mathbf{u}\cdot\mathbf{n}\mathbf{v}\mathrm{d}S, \tag{B2}$$

where $\mathbf{n}$ is the outward unit normal to the surface $\partial\Omega$. With SGS modeling, the molecular kinematic viscosity ν in Eq. (B2) will be replaced by the total viscosity ν_{total} which is the sum of molecular and turbulent viscosities, $\nu_{tot} = \nu + \nu_t$. The closure of the integral of the $2\nu_{tot}\nabla^s\mathbf{u}$ term in $\partial\Omega$ is then related to the wall shear stress,

$$\oint_{\partial\Omega} 2\nu_{tot}\nabla^s\mathbf{u}\cdot\mathbf{n}\mathbf{v}\mathrm{d}S = \oint_{\partial\Omega} \tau_w^{model}\cdot\mathbf{n}\mathbf{v}\mathrm{d}S, \tag{B3}$$

provided by the near-wall model. For stress-free boundary conditions, the obvious outcome is $\nabla^s\mathbf{u} = 0$.

APPENDIX C: GRID SENSITIVITY

The behavior of the wall-damped Smagorinsky model is documented for different grids (refer to Table VI) in the current section. Two methods of grid refinement or coarsening have been considered with respect to the baseline grid: (i) vertical, where the element sizes in the horizontal directions are unaltered; (ii) global, where element sizes in all directions are altered while preserving the aspect ratio of the elements. In both cases, the polynomial order of the basis functions, that is, the number of collocation points per element, is left unchanged. While the vertical grid variation has been applied to all parametric variations of the wall-damped models, the additional global variation of the grid has been tested only for the overdissipative model $C_0^{16}n^2k_c^{4/7}$ and our best performing optimally dissipative model $C_0^{19}n^{05}k_c^{4/7}$. The variation of the filter length scale C_s for different wall-damped Smagorinsky models with grid refinement is shown in Fig. 20. The figure clearly demonstrates that the behavior and the near-wall growth of the coefficient are still preserved for different grids. The slow growth of C_s versus z/Δ in $C_0 = 0.19$, $n = 0.5$ model results in a correct scaling of the filter scales with the grid size Δ showing similar dependence as in a scale-dependant model,[9] while the sharp saturation towards the constant value in the models with $n \geq 1$ makes the variation of C_s with the grid in the near-wall region erroneously less sensitive.

Figure 21 illustrates the variation of normalized streamwise velocity gradient $\Phi(z)$ and streamwise variance $\widetilde{\widetilde{u'^2}}/u_\tau^2$ with wall distance z/H on different grids. The plot illustrates that the physics imposed by the subgrid scale model in the wall-damped Smagorinsky model is more dominant than that imposed by the grid itself. As expected, for cases $C_0^{16}n^2k_c^{4/7}, C_0^{09}n^2k_c^{4/7}, C_0^{17}n^1k_c^{4/7}$, where the *artificial viscous sub-layer* is present, we do observe that refining or coarsening the grids compared to the baseline grid does shift the location of the viscous sub-layer towards or away from the "wall," which is more prominent in the cases of global grid variation, without attenuating or amplifying the peak of the LLM in $\Phi(z)$. This is consistent with the presence of the LES diffusion imposed by the grid size and confirms that the location of "log-layer mismatch" is indeed tied to the grid.[15,20] However, in the case $C_0^{19}n^{05}k_c^{4/7}$, where the log-layer mismatch has been eliminated, the near-wall region is fairly unaffected by the grid variation. In this respect, case $C_0^{19}n^{05}k_c^{4/7}$ is least sensitive to the grids even for second order moments ($\widetilde{\widetilde{u'^2}}$).

To complete the process of performing grid-sensitivity tests, we further plot the energy spectra at different grids in order to illustrate how the variation of physics at multiple scales of motion is affected by the grid sizes. For the normalized 1D u, w energy spectra and uw cospectra (Fig. 22), the scaling laws of the wavenumbers for different parametric models $C_0^{16}n^2k_c^{4/7}$, $C_0^{17}n^1k_c^{4/7}$, $C_0^{09}n^2k_c^{4/7}$, and $C_0^{19}n^{05}k_c^{4/7}$ remain reasonably invariant with the grid coarsening or

TABLE VI. The grid parameters for LES of atmospheric boundary layer. bs is the baseline grid. {v1, bs, v2}—grid sensitivity test in the vertical direction. {g1, bs, g2}—grid sensitivity test in the global domain. Computational domain: $2\pi H \times \pi H \times H$.

Case	$N_x^e \times N_y^e \times N_z^e$	N_{xyz}	Δ_x/Δ_z	Δ_x/Δ_y	$\Delta z/z_0$
v1	$30\times20\times20$	4.19×10^6	4.188	1.33	23
bs	$30\times20\times24$	5.02×10^6	5.0265	1.33	27
v2	$30\times20\times30$	6.27×10^6	5.8543	1.33	32
g1	$20\times13\times16$	1.47×10^6	5.0265	1.33	18
bs	$30\times20\times24$	5.02×10^6	5.0265	1.33	27
g2	$45\times30\times36$	16.87×10^6	5.0265	1.33	40

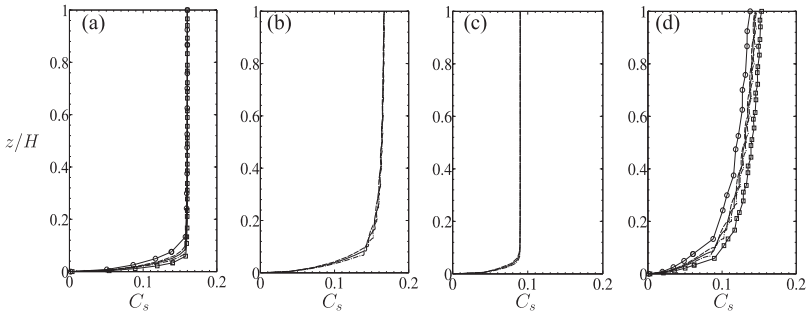

FIG. 20. Filter length scale coefficient C_s of various Smagorinsky models on different grids: (a) case $C_0^{16}n^2k_c^{4/7}$, (b) case $C_0^{17}n^1k_c^{4/7}$, (c) case $C_0^{09}n^2k_c^{4/7}$, and (d) case $C_0^{19}n^{05}k_c^{4/7}$. Vertical grid variation: dashed line—v1, solid line—bs, chain dotted line—v2. Global grid variation [for (a) and (d)]: ○—g1, □—g2. See Table VI for grid details.

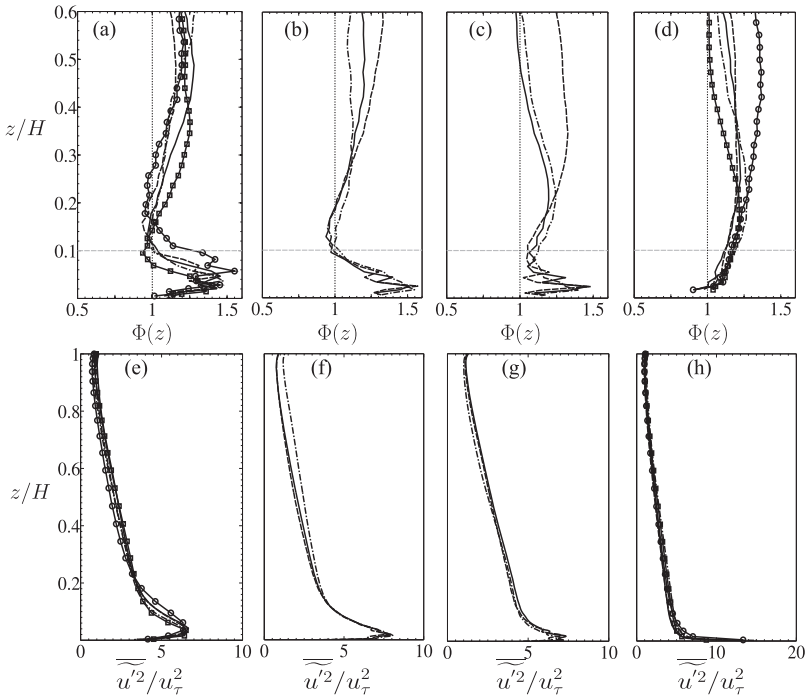

FIG. 21. Normalized streamwise velocity gradient $\Phi(z) = \kappa z/u_\tau dU/dz$ [(a)–(d)] and resolved streamwise variance $\widetilde{u'^2}/u_\tau^2$ [(e)–(h)] for various Smagorinsky models on different grids. [(a) and (e)] Case $C_0^{16}n^2k_c^{4/7}$; [(b) and (f)] Case $C_0^{17}n^1k_c^{4/7}$; [(c) and (g)] case $C_0^{09}n^2k_c^{4/7}$; [(d) and (h)] case $C_0^{19}n^{05}k_c^{4/7}$. Vertical grid variation (spectral elements): dashed line—v1, solid line—bs, chain dotted line—v2. Global grid variation [for (a) and (d)]: ○—g1, □—g2. See Table VI for grid details.

refinement with respect to the baseline grid. Similarly, in the 2D premultiplied streamwise energy spectra reported for cases $C_0^{16}n^2k_c^{4/7}$, $C_0^{19}n^{05}k_c^{4/7}$ in Fig. 23, it is illustrated that the spectral shape (sizes of eddies) at various locations from the wall is preserved for different grids as well. Our best performing model $C_0^{19}n^{05}k_c^{4/7}$ demonstrates the least sensitivity in the scaling and shape of the spectra, even for the global variation of the grids g1, g2 compared to the baseline grid. Furthermore,

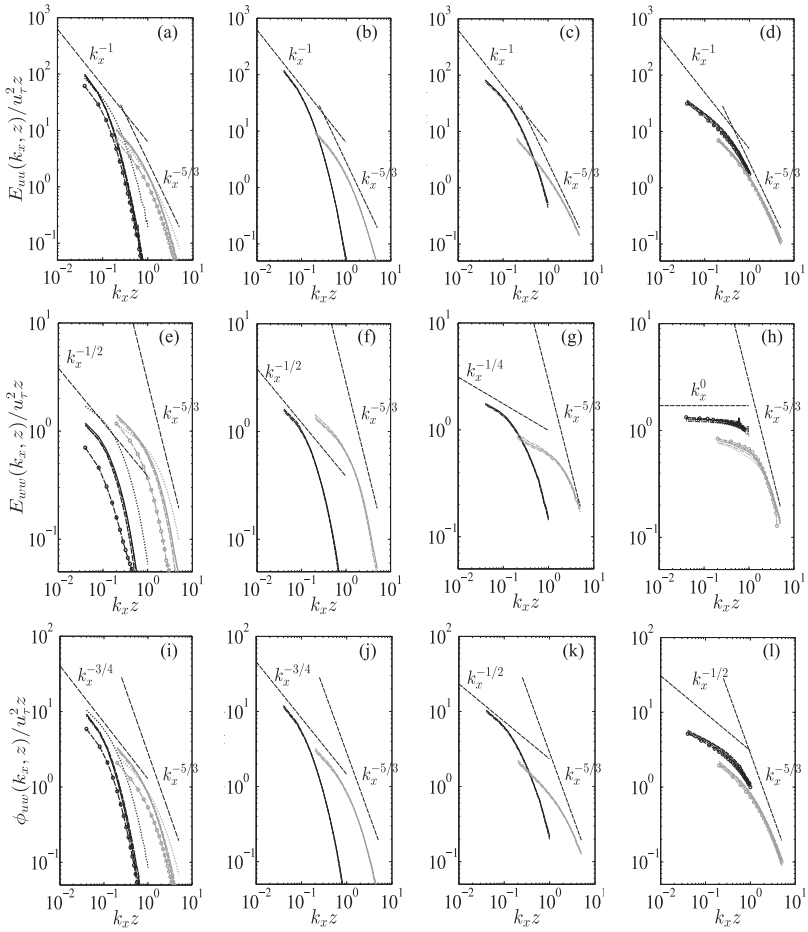

FIG. 22. Normalized streamwise energy spectra, E_{uu} [(a)–(d)], wall-normal energy spectra, E_{ww} [(e)–(h)], and cospectra ϕ_{uw} [(i)–(l)] vs $k_x z$ for various parameters of the wall-damped Smagorinsky model on different grids. [(a), (e), and (i)] case $C_0^{16}n^2k_c^{4/7}$; [(b), (f), and (j)] case $C_0^{17}n^1k_c^{4/7}$; [(c), (g), and (k)] case $C_0^{09}n^2k_c^{4/7}$; [(d), (h), and (l)] case $C_0^{19}n^{05}k_c^{4/7}$. Vertical grid variation: dashed line—v1, solid line—bs, chain dotted line—v2. Global grid variation [for (a) and (d)]: ○—g1, dotted line—g2. See Table VI for grid details.

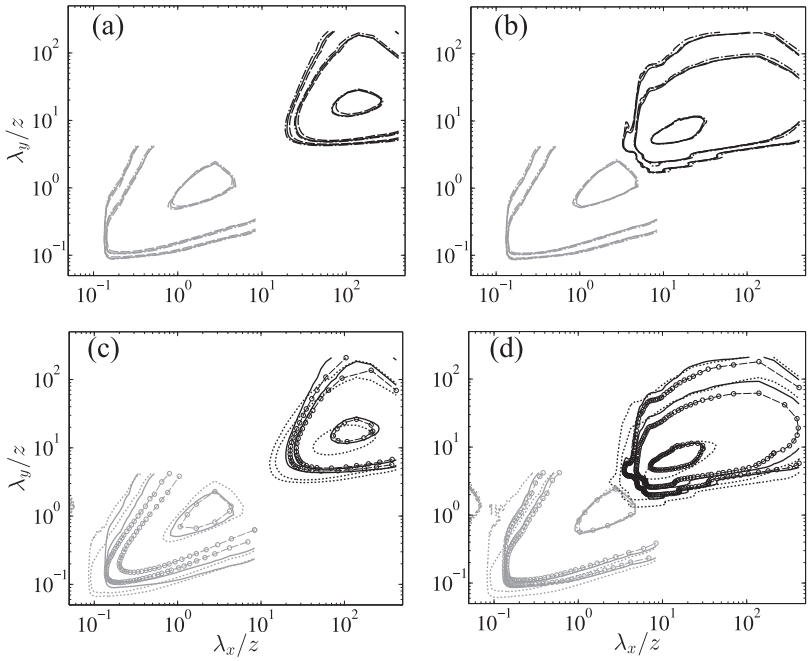

FIG. 23. Premultiplied 2D energy spectra contours $k_x k_y E_{uu}(k_x, k_y, z)/u_\tau^2$ in the λ_x, λ_y plane for two different parametric variations of the wall-damped Smagorinsky model on different grids. $z/H = 0.02$ (black), $z/H = 0.875$ (gray). [(a) and (c)]—Case $C_0^{16} n^2 k_c^{4/7}$; [(b) and (d)]—case $C_0^{09} n^{05} k_c^{4/7}$. Contours at 6.25%, 12.5%, 80% of maximum. Vertical grid variation: dashed line—v1, solid line—bs, chain dotted line—v2. Global grid variation [for (a) and (d)]: ○—g1, dotted line—g2. See Table VI for grid details.

it is worth noting that overdissipative models like $C_0^{16} n^2 k_c^{4/7}$, where the "artificial viscous sublayer" is present, are affected stronger by the global grid variation and consistently manifest a larger variation in spectra, while preserving the shape and the scaling laws.

[1] P. Sagaut, *Large Eddy Simulations for Incompressible Flows* (Springer Verlag, Berlin, 2006).
[2] L. C. Berselli, T. Iliescu, and W. J. Layton, *Mathematics of Large Eddy Simulation of Turbulent Flows* (Springer Verlag, Berlin, 2006).
[3] A. S. Monin and A. M. Obukhov, "Basic laws of turbulent mixing in the ground layer of the atmosphere," Trans. Geophys. Inst. Akad. Nauk. USSR **24**(151), 163–187 (1954).
[4] A. A. Townsend, "Equilibrium layers and wall turbulence," J. Fluid Mech. **11**, 97–120 (1961).
[5] R. Mittal and P. Moin, "Suitability of upwind-biased finite difference schemes for large-eddy simulation of turbulent flows," AIAA J. **35**, 1415–1417 (1997).
[6] J. Smagorinsky, "General circulation experiments with the primitive equations," J. Mon. Weather Rev. **91**, 99–164 (1963).
[7] M. Germano, U. Piomelli, P. Moin, and W. L. Cabot, "A dynamic subgrid-scale eddy viscosity model," Phys. Fluids A **3**, 1760–1765 (1991).
[8] C. Meneveau, T. S. Lund, and W. H. Cabot, "A Lagrangian dynamic sub-grid scale model of turbulence," J. Fluid Mech. **319**, 353–385 (1996).
[9] F. Porté-Agel, C. Meneveau, and M. B. Parlange, "A scale-dependant dynamics model for large eddy simulation: Application to a neutral atmospheric boundary layer," J. Fluid Mech. **415**, 261–284 (2000).
[10] J. Bardina, J. Ferziger, and W. Reynolds, "Improved subgrid scale models for large eddy simulation," AIAA Paper No. 1980-1357, 1980.
[11] S. Stolz and N. A. Adams, "An approximate deconvolution procedure for large-eddy simulations," Phys. Fluids **11**, 1699–1701 (1999).
[12] C. H. Moeng, "A large eddy simulation model for the study of planetary boundary-layer turbulence," J. Atmos. Sci. **41**(13), 2311–2330 (1984).
[13] A. Andrén, A. R. Brown, J. Graf, P. J. Mason, C. H. Moeng, F. T. M. Nieuwstadt, and U. Schumann, "Large-eddy simulation of the neutrally stratified boundary layer: A comparison of four computer codes," Q. J. R. Meteorol. Soc. **120**, 1457–1484 (1994).
[14] P. P. Sullivan, J. C. McWilliams, and C. H. Moeng, "A subgrid-scale model for large-eddy simulation of planetary boundary-layer flows," Boundary-Layer Meteorol. **71**, 247–276 (1994).
[15] S. Khanna and J. G. Brasseur, "Analysis of Monin-Obukhov similarity from large-eddy simulation," J. Fluid Mech. **345**, 251–286 (1997).
[16] P. J. Mason and N. S. Callen, "On the magnitude of the subgrid-scale eddy coefficient in large-eddy simulations of turbulent channel flow," J. Fluid Mech. **162**, 439–462 (1986).
[17] P. J. Mason and D. J. Thomson, "Stochastic backscatter in large-eddy simulations of boundary layers," J. Fluid Mech. **242**, 51–78 (1992).
[18] F. T. M. Nieuwstadt and R. A. Brost, "The decay of convective turbulence," J. Atmos. Sci. **43**, 532–546 (1986).
[19] P. Wu and J. Meyers, "A constraint for subgrid-scale stresses in the logarithmic region of high Reynolds number turbulent boundary layers: A solution to log-layer mismatch problem," Phys. Fluids **25**, 015104 (2013).
[20] J. G. Brasseur and T. Wei, "Designing large eddy simulation of turbulent boundary layer to capture law-of-wall scaling," Phys. Fluids **22**, 021303 (2010).
[21] F. K. Chow, R. Street, M. Xue, and J. H. Ferziger, "Explicit filtering and reconstruction turbulence modeling for large-eddy simulation of neutral boundary layer flow," J. Atmos. Sci. **62**, 2058 (2005).
[22] S. Kawai and J. Larsson, "Wall-modeling in large eddy simulation: Length scales, grid resolution and accuracy," Phys. Fluids **24**, 015105 (2012).
[23] J. Meyers and P. Sagaut, "On the model coefficient for the standard and the variational multi-scale Smagorinsky model," J. Fluid Mech. **569**, 287–319 (2006).
[24] R. J. A. M. Stevens, M. Wilczek, and C. Meneveau, "Large-eddy simulation study of the logarithmic law for second and higher-order moments in turbulent wall-bounded flow," J. Fluid Mech. **757**, 888–907 (2014).
[25] E. Bou-Zeid, C. Meneveau, and M. Parlange, "A scale-dependant Lagrangian dynamic model for large eddy simulation of complex turbulent flows," Phys. Fluids **17**, 025125 (2005).
[26] J. Meyers, "Error-landscape assessment of large eddy simulation: A review of methodology," J. Sci. Comput. **49**, 65–77 (2011).
[27] J. A. Templeton, G. Medic, and G. Kalitzin, "An eddy-viscosity based near-wall treatment for coarse grid large-eddy simulation," Phys. Fluids **17**, 105101 (2005).
[28] N. Hutchins, T. B. Nickels, I. Marusic, and M. S. Chong, "Hot-wire spatial resolution issues in wall-bounded turbulence," J. Fluid Mech. **635**, 103–136 (2009).
[29] A. J. Smits, B. J. Mckeon, and I. Marusic, "High-Reynolds number wall turbulence," Annu. Rev. Fluid Mech. **43**, 353–375 (2011).
[30] J. Jiménez, J. D. Álamo, and O. Flores, "The large-scale dynamics of near-wall turbulence," J. Fluid Mech. **505**, 179–199 (2004).
[31] J. C. Del Álamo, J. Jiménez, P. Zandonade, and R. D. Moser, "Scaling of the energy spectra of turbulent channels," J. Fluid Mech. **500**, 135–144 (2004).
[32] Y. Hwang, "Statistical structure of self-sustaining attached eddies in turbulent channel flow," J. Fluid Mech. **767**, 254–289 (2015).

[33]A. E. Perry, S. Henbest, and M. S. Chong, "Theoretical and experimental studies of wall turbulence," J. Fluid Mech. **165**, 163–199 (1986).
[34]H. O. Kreiss and J. Oliger, "Comparison of accurate methods for the integration of hyperbolic equation," Tellus **24**, 199–215 (1972).
[35]D. Gottileb and S. Orszag, *Numerical Analysis of Spectral Methods: Theory and Applications* (SIAM, 1977).
[36]A. Kravchenko and P. Moin, "On the effect of numerical errors in large eddy simulation," J. Comput. Phys. **131**, 310–322 (1997).
[37]W. Cabot and P. Moin, "Approximate wall boundary conditions in the large-eddy simulation of high Reynolds number flow," Flow, Turbul. Combust. **63**, 269–291 (1999).
[38]J. Larsson, S. Kawai, J. Bodart, and I. Bermejo-Moreno, "Large eddy simulation with modeled wall-stress: Recent progress and future directions," Mech. Eng. Rev. **3**, 15-00418–15-00418 (2016).
[39]J. Jiménez, "Cascades in wall bounded turbulence," Annu. Rev. Fluid Mech. **44**, 27–45 (2012).
[40]A. T. Patera, "A spectral element method for fluid dynamics: Laminar flow in a channel expansion," J. Comput. Phys. **54**, 468–488 (1984).
[41]Y. Maday and A. T. Patera, "Spectral element methods for incompressible Navier-Stokes equations," in *State-of-the-Art Surveys on Computational Mechanics*, edited by A. K. Noor and J. T. Oden (ASME, New York, 1989), Chap. 3, pp. 71–143.
[42]P. Fischer, "An overlapping Schwarz method for spectral element solution of the incompressible Navier-Stokes equations," J. Comput. Phys. **133**, 84–101 (1997).
[43]M. O. Deville, P. F. Fischer, and E. H. Mund, *High-Order Methods for Incompressible Fluid Flow* (Cambridge University Press, Cambridge, UK, 2002).
[44]P. F. Fischer, J. W. Lottes, and S. G. Kerkemeier, "Nek5000: An open source CFD solver," http://nek5000.mcs.anl.gov, 2008.
[45]S. A. Orszag, "Transform method for calculations of vector coupled sums: Application to the spectral form of vorticity equation," J. Atmos. Sci. **27**, 890–895 (1970).
[46]C. M. Canuto, Y. Hussaini, A. Quarteroni, and T. A. Zhang, *Spectral Methods in Fluid Dynamics*, 8th ed. (Springer-Verlag, New York, 1988).
[47]J. W. Deardorff, "A numerical study of three-dimensional turbulent channel flow at large Reynolds number," J. Fluid Mech. **41**, 453–480 (1970).
[48]T. Chatterjee and Y. Peet, "Actuator line wind turbine simulations in atmospheric turbulent flows using spectral element method," AIAA Paper 2015-0727 (2015), 05–09 January 2015, Kissimmmee, Florida.
[49]U. Schumann, "Subgrid scale model for finite difference simulations of turbulent flows in plane channels and annuli," J. Comput. Phys. **18**, 376–404 (1975).
[50]G. Grötzbach, "Direct numerical and large eddy simulations of turbulent channel flows," in *Encyclopedia of Fluid Mechanics*, edited by N. P. Cheremisinoff (Gulf, 1987), pp. 1337–1391.
[51]U. Piomelli, P. Moin, J. H. Freziger, and J. Kim, "New approximate boundary conditions for large-eddy simulations of wall-bounded flows," Phys. Fluids A **1**, 1061–1068 (1989).
[52]H. M. Blackburn and S. Schmidt, "Spectral element filtering techniques for large eddy simulation with dynamic estimation," J. Comput. Phys. **186**, 610–629 (2003).
[53]R. Bouffanais, M. O. Deville, and E. Leriche, "Large-eddy simulation of the flow in a lid-driven cubical cavity," Phys. Fluids **19**, 055108 (2007).
[54]G. Lodato, P. Castonguay, and A. Jameson, "Structural wall-modeled LES using a high-order spectral difference scheme for unstructured meshes," Flow, Turbul. Combust. **92**, 579–606 (2014).
[55]J. B. Chapelier and G. Lodato, "A spectral-element dynamic model for the large-eddy simulation of turbulent flows," J. Comput. Phys. **321**, 279–302 (2016).
[56]M. Calaf, C. Meneveau, and J. Meyers, "Large eddy simulation study of fully developed wind-turbine array boundary layers," Phys. Fluids **22**, 015110 (2010).
[57]J. Kim, P. Moin, and R. Moser, "Turbulence statistics in fully developed channel flow at low Reynolds number," J. Fluid Mech. **177**, 133–166 (1987).
[58]S. B. Pope, *Turbulent Flows* (Cambridge Press, 2000).
[59]S. Hoyas and J. Jiménez, "Scaling of velocity fluctuations in turbulent channels up to $Re_\tau = 2003$," Phys. Fluids **18**, 011702 (2006).
[60]M. Lee and R. D. Moser, "Direct numerical simulation of turbulent channel flow up to $Re_\tau = 5200$," J. Fluid Mech. **774**, 395–415 (2015).
[61]A. E. Perry and I. Marušic, "A wall-wake model for the turbulence structure of boundary layers. Part 1. Extension of the attached eddy hypothesis," J. Fluid Mech. **298**, 361–388 (1995).
[62]R. J. Adrian, "Hairpin vortex organization in wall turbulence," Phys. Fluids **19**, 041301 (2007).
[63]B. J. Balakumar and R. J. Adrian, "Large and very-large-scale motions in channel and boundary-layer flows," Philos. Trans. R. Soc., A **365**, 665–681 (2007).
[64]M. Guala, S. E. Hommema, and R. J. Adrian, "Large-scale and very-large-scale motions in turbulent pipe flow," J. Fluid Mech. **554**, 521–642 (2006).
[65]J. H. Lee and H. J. Suang, "Comparison of very-large-scale motions of turbulent pipe and boundary layer simulations," Phys. Fluids **25**, 045103 (2013).
[66]J. Laufer, *The Structure of Turbulence in Fully Developed Pipe Flow* (NACA, 1953); available at https://ntrs.nasa.gov/archive/nasa/casi.ntrs.nasa.gov/19930083.
[67]J. F. Morrison, W. Jiang, B. J. Mckeon, and A. J. Smits, "Reynolds number dependence of streamwise velocity spectra in turbulent pipe flow," Phys. Rev. Lett. **88**, 214501 (2002).
[68]M. Hites, "Scaling of high-Reynolds number turbulent boundary layers in the National Diagnostic Facility," Ph.D. thesis, Illinois Institute of Technology, Chicago, 1997.
[69]I. Marušic and A. E. Perry, "A wall-wake model for the turbulence structure of boundary layers. Part 2. Further experimental support," J. Fluid Mech. **298**, 389–407 (1995).
[70]T. B. Nickels, I. Marusic, S. Hafez, and M. S. Chong, "Evidence of the k^{-1} law in a high-Reynolds-number turbulent boundary layer," Phys. Rev. Lett. **95**, 074501 (2005).
[71]T. B. Nickels, I. Marusic, S. Hafez, N. Hutchins, and M. S. Chong, "Some predictions of the attached eddy model for a high Reynolds number boundary layer," Philos. Trans. R. Soc., A **365**, 807–822 (2007).
[72]B. A. Kader and A. M. Yaglom, "Spectra and correlation functions of surface layer atmospheric turbulence in unstable thermal stratification," in *Turbulence and Coherent Structures*, edited by O. Métais and M. Lesieur (Kluwer, 1991).
[73]G. G. Katul, C. R. Chu, M. B. Parlange, J. D. Albertson, and T. A. Ortenburger, "Low-wavenumber spectral characteristics of velocity and temperature in the atmospheric boundary layer," J. Geophys. Res. **100**, 14243–14255, doi:10.1029/94jd02616 (1995).
[74]K. G. Mcnaughton, "Attached eddies and production spectra in atmospheric logarithmic layer," J. Fluid Mech. **111**, 1–18 (2004).
[75]G. J. Kunkel and I. Marusic, "Study of the near-wall-turbulent region of the high-Reynolds-number boundary layer using an atmospheric flow," J. Fluid Mech. **548**, 375–402 (2006).
[76]G. G. Katul, J. D. Albertson, C. I. Hsie, P. S. Konklin, J. T. Sigmon, M. B. Parlange, and K. R. Knoerr, "The 'inactive' eddy motion and the large scale turbulent pressure fluctuations in the dynamic sublayer," J. Atmos. Sci. **53**, 2512–2524 (1996).
[77]J. F. Morrison, "The interaction between inner and outer regions of turbulent wall-bounded flow," Philos. Trans. R. Soc., A **365**, 683–698 (2007).
[78]A. E. Perry and J. D. Li, "Experimental support for the attached eddy hypothesis in zero- pressure-gradient turbulent boundary layers," J. Fluid Mech. **218**, 405–438 (1990).
[79]K. A. Flack, M. P. Schultz, and T. A. Shapiro, "Experimental support for Townsend's Reynolds number similarity hypothesis on rough walls," Phys. Fluids **17**, 035102 (2005).
[80]J. Jiménez, "Turbulent flow over rough walls," Annu. Rev. Fluid Mech. **36**, 173–196 (2004).
[81]G. G. Katul, A. Porporato, S. Shah, and E. Bou-Zeid, "Two phenomenological constants explain similarity laws in stably stratified turbulence," Phys. Rev. E **89**, 023007 (2014).
[82]S. G. Saddoughi and S. V. Veeravalli, "Local isotropy in turbulent boundary layers at high Reynolds number," J. Fluid Mech. **268**, 333–372 (1994).
[83]G. G. Katul, A. Porporato, C. Manes, and C. Meneveau, "Co-spectrum and mean velocity in turbulent boundary layers," Phys. Fluids **25**, 091702 (2013).
[84]S. Hoyas and J. Jiménez, "Reynolds number effects on the Reynolds-stress budgets in turbulent channels," Phys. Fluids **20**, 101511 (2008).
[85]K. J. Bullock, R. E. Cooper, and F. H. Abernathy, "Structural similarity in radial correlations and spectra of longitudinal velocity fluctuations in pipe flow," J. Fluid Mech. **88**, 585–608 (1978).
[86]A. Bershadskii, E. Kit, A. Tsinober, and H. Vaisburd, "Strongly localized events of energy, dissipation, enstrophy and enstrophy generation in turbulent flows," Fluid Dyn. Res. **14**, 71 (1994).

[87]S. Chen, K. R. Sreenivasan, and M. Nelkin, "Inertial range scalings of dissipation and enstrophy in isotropic turbulence," Phys. Rev. Lett. **79**, 1253–1256 (1997).
[88]A. W. Vreman, "An eddy viscosity subgrid-scale model for turbulent shear flow: Algebraic theory and applications," Phys. Fluids **16**, 3670–3681 (2004).
[89]F. Nikoud and F. Ducros, "Subgrid-scale stress modelling based on the square of the velocity gradient tensor," Flow, Turbul. Combust. **62**, 183–200 (1999).
[90]F. Nicoud, H. B. Toda, O. Cabrit, S. Bose, and J. Lee, "Using singular values to build a subgrid-scale model for large eddy simulations," Phys. Fluids **23**, 085106 (2011).
[91]J. Jiménez and A. Pinnelli, "The autonomous cycle of near wall turbulence," J. Fluid Mech. **389**, 335–359 (1999).
[92]S. Rawat, C. Cossu, Y. Hwang, and F. Rincon, "On the self-sustained nature of large-scale motions in turbulent Couette flow," J. Fluid Mech. **782**, 515–540 (2015).
[93]J. P. Boyd, "Two comments on filtering (artificial viscosity) for Chebyshev and Legendre spectral and spectral element methods: Preserving boundary conditions and interpretation of the filter as diffusion," J. Comput. Phys. **143**, 283–288 (1998).
[94]R. E. Lynch and J. R. Rice, "Direct solution of partial difference equations by tensor product methods," Numer. Math. **6**, 185–199 (1964).